Bachelorarbeit

zur Erlangung des Hochschulgrades
Bachelor of Science
im Bachelor-Studiengang Physik

Study of the Effects of Anomalous Quartic Gauge Couplings on the Scattering of Two Gauge Bosons $VV \rightarrow VV$ at the Large Hadron Collider

Carsten Bittrich

geboren am 09.02.1989 in Görlitz

Technische Universität Dresden
Institut für Kern- und Teilchenphysik
Fachrichtung Physik
Fakultät Mathematik und Naturwissenschaften

17.12.2012

Eingereicht am 17. Dezember 2012

1. Gutachter:	Prof. Dr. M. Kobel
2. Gutachter:	Prof. Dr. D. Stöckinger

Zusammenfassung

In dieser Bachelorarbeit wird der Einfluss verschiedener Parametrisierungen einer effektiven Theorie auf die Streuung von Vektorbosonen untersucht. Dazu wurden Samples auf "Generator-Level" mit den Monte-Carlo Generatoren VBFNLO und WHIZARD simuliert und mittels des Analysetools RIVET verglichen. Die Einflüsse der aQGC Parameter f_i und α_i einer effektiven Lagrange-Dichte wurden untersucht um in späteren Analysen Grenzen auf diese zu setzen. Außerdem wurde versucht eine Umrechnung zwischen diesen Parametern zu finden und mit der aus der Theorie hervorgesagten [1] Umrechnung verglichen. Dabei wurden zwei verschiedene Unitarisierungs-Methoden verglichen.

Eine Umrechnung zwischen diesen Parametern war möglich, obwohl ein großer Einfluss der Unitarisierung beobachtet wurde. Die vorhergesagte Umrechnung konnte nicht bestätigt werden, da der totale Wechselwirkungsquerschnitt ein nichtkompatibles Verhalten gezeigt hat.

Abstract

In this thesis, the influences of different parametrizations of an effective theory on Vector Boson Scattering were studied. Samples on "generator level" were simulated with VBFNLO and WHIZARD and compared using the analysis tool RIVET. The influences of the aQGC parameters f_i and α_i of an effective Lagrangian were studied to set limits on them in further studies. Furthermore a conversion between them was tried to be found and compared to a prediction [1]. Two different unitarizations were compared.

A conversion of the different parametrizations was possible although a strong effect of the unitarization method was observed. The predicted conversion was not confirmed, since the dependencies of the total cross sections showed a behaviour not compatible.

Contents

Chapter 1

Introduction

Particle physicists try to discover and study the elementary particles of matter and their interactions. In the last century a theory was developed to describe this, being known as the Standard Model of particle physics. Up to now it is well tested and in a good agreement with experimental measurements. History has shown that a theory might be obsolete once new regions of accuracy of measurement as well as higher energies become available. Thus an important interest of particle physicist is to determine the borders of validity of the Standard Model and to test whether these new models of physics have indirect and direct effects on the experimental available energy ranges. By comparing measured distributions with the prediction of the Standard Model one can set limits on parametrizations of these effects.

The Standard Model predicts an interaction of the electroweak gauge bosons called Vector Boson Scattering. The prediction of the Standard Model without a Higgs boson would lead to a breaking of the unitarity. Therefore this process is important for the study of the way electroweak symmetry is broken and of the properties of the Higgs boson.

For that reason the influences of two different parametrizations on Vector Boson Scattering was studied in this thesis. Another aim is to find a possible conversion between two different parametrizations to work with in further studies.

In chapter 2 the Standard Model and two different parametrizations are introduced. Chapter 3 explains the experiment collecting data for a later comparison. In chapter 4 the way of simulating data is described. This simulated data is validated in chapter 5. In chapter 6 the influences of the parametrizations on the total cross sections are studied. Chapter 7 compares the influences on the differential cross sections. A study of the conversion of the used parametrizations is shown in chapter 8 and a summary is given in chapter 9.

Chapter 2

Theoretical Framework

2.1 The Standard Model

The Standard Model of particle physics (SM) is a successful theory describing physical processes. It is comprised of a theory for elementary particles, the fundamental constituents of matter, and their interactions [2, 3]. It is well-tested and in good agreement with experimental results.

Up to now four fundamental interactions are known. The gravitational force is the only interaction that is not included in the Standard Model. The three remaining interactions, the strong interaction described by quantum chromodynamics, the electromagnetic interaction described by quantum electrodynamics and the weak interaction are included in the Standard Model. Glashow, Salam and Weinberg [2, 3, 4] have been able to find a theory that combines both the electromagnetic and the weak interactions: the electroweak theory.

According to the Standard Model elementary particles are divided into two groups, fermions and bosons. Fermions (see table 2.1) are particles following Fermi-Dirac statistics with a half-integer spin and can be subdivided into leptons and quarks. Three generations of fermions are known, each containing one electromagnetically charged lepton with an absolute charge 1, one neutral lepton, two quarks and the corresponding anti-particles. The up-type quark has an absolute electromagnetic charge of $+\frac{2}{3}$ and the down-type quark has an absolute charge of $\frac{1}{3}$. The different generations differ only in particle masses. The charge the electroweak interaction couples to is called weak isospin and depends on the chirality of a given particle.

Bosons (see table 2.2) are integer spin particles obeying Bose-Einstein statistics. In the Standard Model bosons are the mediators of the interaction between particles, described by local gauge theory. Thus these bosons are called gauge bosons. Gluons carry the strong force and photons the electromagnetic force. The Z^0 and the $W^\pm$ bosons are the gauge bosons of the weak force. These bosons have a spin of 1 and are also called vector bosons, whereas the Higgs boson H is a scalar boson with a spin of 0. It is an excitation of the Higgs field, which is assumed to be[1] responsible for the electroweak symmetry breaking (see section 2.1.2).

Since the electroweak gauge theory describes vector boson scattering, it is of higher importance for this thesis and a closer look at it is taken.

2.1.1 Electroweak gauge theory

The electroweak gauge theory by Glashow, Salam and Weinberg [2, 3, 4] describes particles as left- and right-handed four component Dirac fermion fields:

$$\phi_{L/R} = \frac{1}{2}\left(1 \mp \frac{\gamma^5}{2}\right)\phi \tag{2.1}$$

[1]It is necessary in SM, but was not experimantally verified jet. However is is assumed to have been measured [6].

Generation		Fermion	Electric charge	Weak isospin $\|T_3\|$ left-handed	right-handed	Mass m in MeV
1st	e^-	electron	-1	$1/2$	0	0.511
	ν_e	electron-neutrino	0	$1/2$	none	$< 2 \cdot 10^{-6}$
	u	up	$2/3$	$1/2$	0	$2.3^{+0.7}_{-0.5}$
	d	down	$-1/3$	$1/2$	0	$4.8^{+0.7}_{-0.3}$
2nd	μ^-	muon	-1	$1/2$	0	105.7
	ν_μ	muon-neutrino	0	$1/2$	none	$< 2 \cdot 10^{-6}$
	c	charm	$2/3$	$1/2$	0	1275 ± 25
	s	strange	$-1/3$	$1/2$	0	95 ± 5
3rd	τ^-	tau	-1	$1/2$	0	1177
	ν_τ	tau-neutrino	0	$1/2$	none	$< 2 \cdot 10^{-6}$
	t	top	$2/3$	$1/2$	0	$(1.735 \pm 0.014) \cdot 10^5$
	b	bottom	$-1/3$	$1/2$	0	$(4.18 \pm 0.03) \cdot 10^3$

Table 2.1: List of fermions in the Standard Model sorted by the generation. The first two lines of every generation represent the leptons, whereas the later two lines are the quarks. Each listed particle has a anti-particle with opposite charge. Data are taken from [5].

	Boson	Electric charge	Spin	Interaction	Mass m in GeV
γ	photon	0	1	electromagnetic	$< 1 \cdot 10^{-27}$
$W^\pm$	W bosons	± 1	1	weak	80.385 ± 0.015
Z^0	Z boson	0	1	weak	91.188 ± 0.002
g	gluons	0	1	strong	0
H	Higgs	0	0		115.5 and none $127 - 600$ GeV

Table 2.2: List of bosons in the Standard Model sorted by spin. First four lines represent vector bosons while the Higgs boson in the last line is a scalar boson. Data taken from [5].

with one of the Dirac matrices γ^5. This theory contains a $SU(2)_L \times U(1)_Y$ symmetry and the full Lagrangian is given by

$$\mathcal{L} = i\bar{L}^j_L \gamma^\mu D_\mu L^j_L + i\bar{l}^j_R \gamma^\mu D_\mu l^j_R + \bar{Q}^j_L \gamma^\mu D_\mu Q^j_L + i\bar{u}^j_R \gamma^\mu D_\mu u^j_R \tag{2.2}$$

$$+ i\bar{d}^j_R \gamma^\mu D_\mu d^j_R - \frac{1}{4} W_{a,\mu\nu} W^{\mu\nu}_a - \frac{1}{4} B_{\mu\nu} B^{\mu\nu} \, . \tag{2.3}$$

Einsteins summing convention is applied and the adjoint spinor is defined as $\bar{\phi} := \phi^\dagger \gamma^0$. For left-handed vector fields the doublet notation is used and j is an index of the generations. Using the covariant derivative

$$D_\mu = \partial_\mu + i g_W T_a W^a_\mu + i g_Y Y B_\mu \tag{2.4}$$

ensures local gauge invariance under the $SU(2)_L \times U(1)_Y$ transformation

$$\psi \rightarrow e^{i(\alpha(x) Y + \beta_a(x) T_a)} \psi \, . \tag{2.5}$$

With the weak isospin $T_a \equiv \frac{1}{2}\sigma_a$ (σ_a – Pauli matrices), the weak hypercharge $Y = Q - T_3$ and the gauge couplings of the gauge fields W^a_μ ($a = 1, 2, 3$) and B_μ, g_W and g_Y.

The last two terms in the Lagrangian are the kinetic terms of the gauge bosons where the field strength tensors are defined by

$$B_{\mu\nu} = \partial_\mu B_\nu - \partial_\nu B_\mu \tag{2.6}$$

$$W^a_{\mu\nu} = \partial_\mu W^a_\nu - \partial_\nu W^a_\mu + g_W \epsilon^{abc} W^b_\mu W^c_\nu \tag{2.7}$$

using the gauge fields.

These gauge fields can be identified with the physical gauge bosons using the following equations:

$$\begin{pmatrix} A_\mu \\ Z_\mu \end{pmatrix} = \begin{pmatrix} \cos\theta_W & \sin\theta_W \\ -\sin\theta_W & \cos\theta_W \end{pmatrix} \begin{pmatrix} B_\mu \\ W^3_\mu \end{pmatrix} \tag{2.8}$$

$$W^\pm_\mu = \frac{1}{\sqrt{2}}(W^1_\mu \mp iW^2_\mu)\,. \tag{2.9}$$

This means the photon γ and the Z^0 boson result from a rotation by the so called electroweak mixing angle or Weinberg angle θ_W of the gauge fields B_μ and W^3_μ and both charged W_μ fields are linear combinations of W^1_μ and W^2_μ.

2.1.2 Electroweak symmetry breaking (EWSB)

One Problem of the electroweak theory is, that all particles are assumed to be massless. Mass terms are not invariant under the transformation given in (2.5) and therefore break the $SU(2)_L \times U(1)_Y$ symmetry. This is solved by the *electroweak symmetry breaking* via the Higgs mechanism [7, 8]. It predicts a symmetrical Higgs field with a non-invariant lowest energy state. This would give masses to bosons and fermions would gain mass by interacting with this Higgs field. The Higgs field can only be observed indirectly, through its excitation – the Higgs boson H. The Standard Model requires such a Higgs boson and in 2012, after 40 years of search, CERN announced they had found a new particle which is compatible with the Standard Model Higgs boson [6].

But there are also more general approaches for electroweak symmetry breaking, e. g. by a Σ field [9]. The Higgs field is a special case of a Σ field.

2.2 Vector Boson Scattering

To study the electroweak symmetry breaking, Vector Boson Scattering (VBS) is a very important process aimed to be measured at the LHC. Furthermore Vector Boson Scattering includes triple and quartic gauge couplings and Higgs channels. In this process gauge bosons, emitted by quarks from each proton, interact with each other and decay afterwards (see figure 2.1).

There are several possible channels for the interaction between the gauge bosons. The Standard Model predicts a quartic boson coupling or the exchange of a γ or Z^0 gauge boson or a Higgs boson (see figure 2.2).

Vector Boson Scattering requires six weak vertices, so it is a $\mathcal{O}(\alpha_W^6)$ process with a small cross section compared to most of the processes observed at the LHC. Due to experimental limitations it was not yet observed.

A very important experimental signature of Vector Boson Scattering are the two jets in the forward pseudorapidity region, called tagging jets, resulting from the quarks emitting the gauge bosons. So the pseudorapidity difference of the jets $|\Delta\eta_{jj}|$ is expected to be rather large. In most analyses only the leptonic decay channels of the bosons are considered to have less background from multi-jet events contaminating the signal region. The leptons from the decaying bosons tend to be in a pseudorapidity region spanned by the tagging jets. This is measured by the lepton centrality $\zeta_{\ell\ell}$ defined as:

$$\zeta_{\ell\ell} \equiv \min\left\{\min\{\eta^\ell_1, \eta^\ell_2\} - \min\{\eta^j_1, \eta^j_2\}, \max\{\eta^j_1, \eta^j_2\} - \max\{\eta^\ell_1, \eta^\ell_2\}\right\}\,. \tag{2.10}$$

A scheme of a characteristic event is shown in figure 2.4.

In this thesis only the same sign W^+W^+ (`WWss`) and the W^+Z^0 (`WZ`)[2] channels are considered. For sake of simplicity only one flavor was generated, so the corresponding final

[2]This channel also includes the $W^+\gamma^*$ channel, since it is not distinguishable to the pure `WZ` channel.

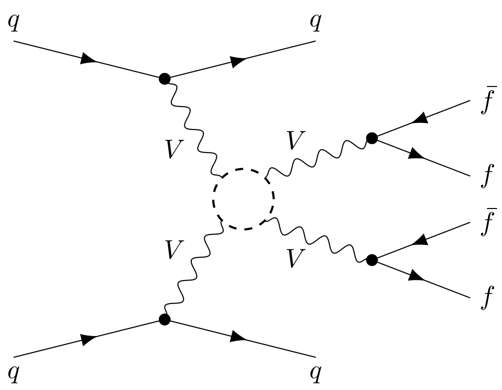

Figure 2.1: Feynman graph of a general VBS process. Straight lines with arrows represent fermions. Curved lines represent vector bosons. Dashed circle stands for the different possibilities of interactions between the vector bosons shown in figure 2.2.

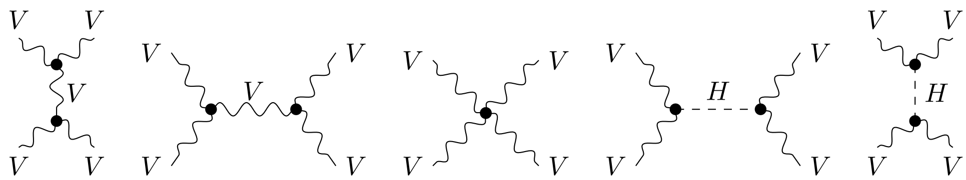

Figure 2.2: Feynman graphs for all possible VBS channels. Initial and final state as shown in figure 2.1

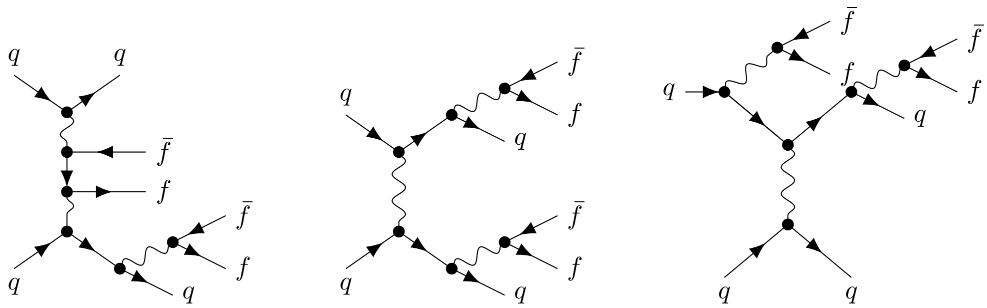

Figure 2.3: Feynman graphs of other processes with the same final state as VBS. These are not gauge invariantly separable processes.

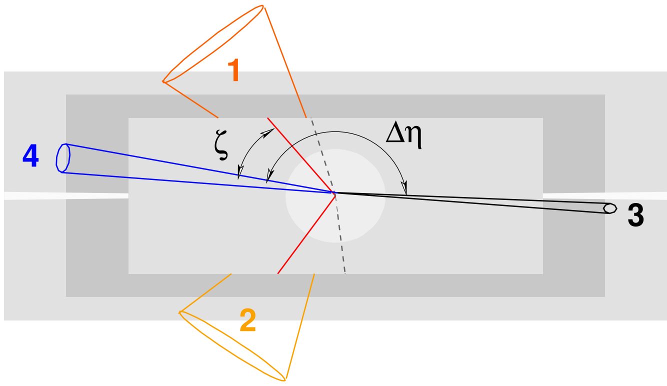

(a) R-η plane

Figure 2.4: Schematic view of a Vector Boson Scattering event in the ATLAS detector. 1 and 2 are leptons and 3 and 4 are jets. Observables $\Delta\eta_{jj}$ and ζ_{ll} as described in the text are shown. Graph is taken from [10].

states are

$$jje^+\nu_e e^+\nu_e\,, \qquad\qquad jje^+e^-e^+\nu_e\,. \tag{2.11}$$

There are other $\mathcal{O}(\alpha_W^6)$ processes with the same final state which are not gauge invariantly separable. Those processes (see figure 2.3) are included in the used samples.

2.3 Anomalous quartic gauge coupling (aQGC)

Up to now the Standard Model shows good agreement with experiments. However it is possible that this is only correct up to an unknown center of mass energy scale Λ. New effects or completely new physics could occur beyond this energy with indirect or direct effects on the currently experimental accessible energy range. One way to study this is to build an effective field theory [1] to parametrize these effects on the low energy regions. This introduces more degrees of freedom to the Standard Model.

One approach is to build an effective Lagrangian with additional operators of higher dimension[3]

$$\mathcal{L}_{\text{eff}} = \mathcal{L}_{\text{SM}} + \sum_i \frac{c_i}{\Lambda_i}\mathcal{O}_i \tag{2.12}$$

with the parameter c_i. Due to this higher dimension these operators $\mathcal{O}$ have coefficients of inverse power of mass so the operators with the lowest dimension are dominant. Most of the SM operators are of dimension four and since only operators with even dimension satisfy conservation of lepton and baryon number[4] the new operators have to be at least dimension six operators. These new operators effect also double and triple gauge boson couplings; these can be studied more easily in other processes.

Dimension eight operators have no effects in double or triple couplings so they have to be searched for in quartic gauge couplings. Vector Boson Scattering allows these examinations. In general the following are the possible operators for the quartic gauge boson vertex

$$\mathcal{O}_0^{WW} = g^{\alpha\beta}g^{\gamma\delta}[W_\alpha^+ W_\beta^- W_\gamma^+ W_\delta^-] \qquad \mathcal{O}_1^{WW} = g^{\alpha\beta}g^{\gamma\delta}[W_\alpha^+ W_\beta^+ W_\gamma^- W_\delta^-] \tag{2.13}$$

$$\mathcal{O}_0^{WZ} = g^{\alpha\beta}g^{\gamma\delta}[W_\alpha^+ Z_\beta W_\gamma^- Z_\delta] \qquad \mathcal{O}_1^{WZ} = g^{\alpha\beta}g^{\gamma\delta}[W_\alpha^+ W_\gamma^- Z_\beta Z_\delta]\,. \tag{2.14}$$

[3]Dimension in this context is the power of mass which is determined by dimensional analysis of the Lagrangian.

[4]Proof can be found in [11].

With equation (2.12) they lead to an effective Lagrangian of the quartic vertex

$$\mathcal{L}^{VVV'V'} = c_0^{VV'} \mathcal{O}_0^{VV'} + c_1^{VV'} \mathcal{O}_1^{VV'} \,. \tag{2.15}$$

In the Standard Model renormalizability and gauge invariance under the $SU(2)_L$ symmetry imply that

$$c_{0,\mathrm{SM}}^{WW} = -c_{1,\mathrm{SM}}^{WW} = \frac{2}{\cos^2\theta_W} c_{0,\mathrm{SM}}^{WZ} = -\frac{2}{\cos^2\theta_W} c_{1,\mathrm{SM}}^{WZ} = g_W^2 \,. \tag{2.16}$$

If operators of higher order are included these coefficients differ by an additional term.

$$c_i^{VV'} = c_{i,\mathrm{SM}}^{VV'} + g^2 \Delta c_i^{VV'} \,. \tag{2.17}$$

For simplicity's sake only the operators not including derivatives of the gauge fields are considered here. There are two possibilities to define these operators depending on the way the electroweak symmetry is broken.

If the electroweak symmetry is linearly broken by a Higgs field including a light Higgs boson only two operators are possible

$$\mathcal{L}_{s,0} = \frac{f_0}{\Lambda^4} \left[(D_\mu\Phi)^\dagger D_\nu \Phi\right] \times \left[(D^\mu\Phi)^\dagger D^\nu \Phi\right] \tag{2.18}$$

$$\mathcal{L}_{s,1} = \frac{f_1}{\Lambda^4} \left[(D_\mu\Phi)^\dagger D_\mu \Phi\right] \times \left[(D^\nu\Phi)^\dagger D^\nu \Phi\right] \tag{2.19}$$

using the Higgs doublet field Φ and its covariant derivative $D_\mu\Phi$. These operators lead to the following variations of the coefficients

$$\begin{aligned} \Delta c_i^{WW} &= \frac{g^2 v^4 f_i}{8\Lambda^4} \equiv \Delta c_{i,\mathrm{lin}} \\ \Delta c_i^{WZ} &= \frac{g^2 v^4 f_i}{16\cos^4\theta_W \Lambda^4} = \frac{\Delta c_{i,\mathrm{lin}}}{2\cos^2\theta_W} \,. \end{aligned} \tag{2.20}$$

using the vacuum expectation value v and the energy scale Λ. If EWSB is due to a heavy Higgs boson or without a Higgs boson one has to follow a more general approach using a Σfield for a non-linear realization of the EWSB. It can be shown that the energy scale Λ must be below $4\pi v \approx 3\,\mathrm{TeV}$.

Only 2 operators fulfill $SU(2)$ symmetry

$$\mathcal{L}_4^{(4)} = \alpha_4 [\mathrm{Tr}(V_\mu V_\nu)]^2 \,, \tag{2.21}$$

$$\mathcal{L}_5^{(4)} = \alpha_5 [\mathrm{Tr}(V_\mu V^\mu)]^2 \,, \tag{2.22}$$

using $V_\mu \equiv (D_\mu \Sigma)\Sigma$. These generate four gauge boson interactions with

$$\begin{aligned} \Delta c_i^{WW} &= g^2 \alpha_{i+4} \equiv \Delta c_{i,\text{no-lin}} \\ \Delta c_i^{WZ} &= \frac{g^2}{2\cos^2\theta_W} \alpha_{i+4} = \frac{\Delta c_{i,\text{no-lin}}}{2\cos^2\theta_W} \,. \end{aligned} \tag{2.23}$$

Using equations (2.20) and (2.23) one finds the following relation

$$\begin{aligned} g^2 \alpha_{i+4} = \Delta c_{i,\text{no-lin}} = \Delta c_{i,\mathrm{lin}} &= \frac{g^2 v^4 f_i}{8\Lambda^4} \\ \alpha_{i+4} &= \frac{v^4 f_i}{8\Lambda^4} \,. \end{aligned} \tag{2.24}$$

To make this independent from this energy scale Λ a new parameter $\tilde{f}_i$ is introduced as

$$\tilde{f}_i \equiv f_i \cdot \frac{\mathrm{TeV}^4}{\Lambda^4} \,. \tag{2.25}$$

This changes equation (2.24) to

$$\alpha_{i+4} = \frac{v^4}{8\,\mathrm{TeV}^4} \tilde{f}_i \approx 4.59 \cdot 10^{-4} \cdot \tilde{f}_i \,. \tag{2.26}$$

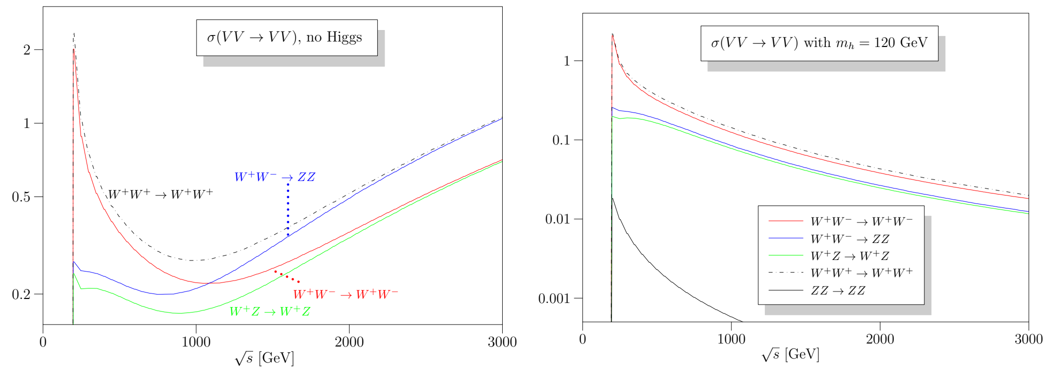

Figure 2.5: Cross sections for different Vector Boson Scattering processes. Left: Without a Higgs boson. Right: With SM-Higgs boson of mass 120 GeV. Graphics taken from [9].

2.4 Unitarity

The Standard Model without a Higgs boson predicts a raise of the Vector Boson Scattering cross section for high energies. This would imply a divergence of the cross section in the high energy regions and therefore break unitarity [12, 9]. Although it was not modeled to do so a light Higgs boson would prevent the divergence and thus restore unitarity (see figure 2.5).

The additional operators of an effective Lagrangian, as explained in section 2.3 lead to a significant change of the effects for high energies and can therefore break unitarity again. Thus an additional unitarization mechanism is needed to restore unitarity. This can be done by slightly changing some properties of the Higgs boson or by other unknown effects of the new physics. Either way real processes obey the unitarity requirement.

However in Monte-Carlo generated samples (see chapter 4) unitarity will be broken due to the missing higher orders and not knowing the unitarization method of nature. For comparability's sake unitarization has to be done by other mechanisms to avoid a large overestimation of the high energy cross sections. Therefore a criterion is needed to test whether the unitarization was successful or not. The optical theorem of scattering theory [12] implies that unitarity is fulfilled if the normalized eigenamplitude $a_{IJ} = \frac{1}{32\pi} A_{IJ}$ of the spin I and weak isospin J fulfills the following equations

$$|\mathrm{Im}\ a_{IJ}| \leq 1 \qquad\qquad |\mathrm{Re}\ a_{IJ}| \leq \frac{1}{2}\,. \tag{2.27}$$

There are several ways to ensure these relations. The following sections will shortly present the two approaches being used in this thesis.

2.4.1 Unitarization by the use of form factors

The general approach of the form factor method is to multiply a function of the center of mass energy to suppress high energy events. VBFNLO (see section 4.1.1), one of the used generators has implemented this approach using the function (see figure 2.6)

$$\mathcal{F} = \left(1 + \frac{m(WW)^2}{\Lambda_{\mathrm{FF}}^2}\right)^{-n} \tag{2.28}$$

with the parameters Λ_{FF} and n. This implements a soft cut off. The parameter n should be greater than 1, in this thesis $n = 2$ is used, and determines the shape of the function. Λ_{FF} on the other hand defines the energy scale for the cut off and has to be adjusted to each situation so that the projections of the matrix element on the zeroth partial wave fulfills equation (2.27). This chosen value for Λ_{FF} is also used for all higher order partial waves. Since the absolute value of the higher order partial waves are always smaller, unitarity is given for all partial waves. The maximum Λ_{FF} for the used anomalous quartic gauge coupling f_i were tested by the authors of VBFNLO and can be found in table 2.3 [13].

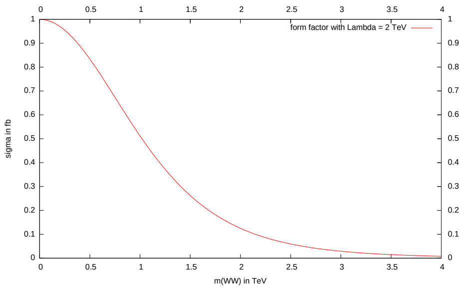

Figure 2.6: Shape of implemented form factor using the parameters $\Lambda_{FF} = 2\,\text{TeV}$ and $n = 2$.

$\left\|\tilde{f}_i\right\|$	$\Lambda_{FF}/\,\text{GeV}$
108.8	905
217.7	755
435.3	637
653.1	579
870.7	543
1500.0	500

Table 2.3: Used values for $\left|\tilde{f}_i\right|$ and corresponding Λ_{FF}.

2.4.2 Unitarization via k matrix method

A sufficient criterion for equation (2.27) is that the spin-isospin eigenamplitudes have to be inside the Argand circle in the complex plane. This corresponds to the relation

$$\left|a_{IJ} - \frac{i}{2}\right| \leq \frac{1}{2}\,. \tag{2.29}$$

The k matrix approach restores unitarity by projecting every partial wave onto the Argand-circle (see figure 2.7) using the relation [9]

$$\tilde{a}_{IJ} = \frac{1}{\text{Re}(1/a_{IJ}) - i} = \frac{a_{IJ}}{1 - i a_{IJ}}\,. \tag{2.30}$$

An important difference to the form factor method is that higher order partial waves and thus the total cross sections are in generall less suppressed.

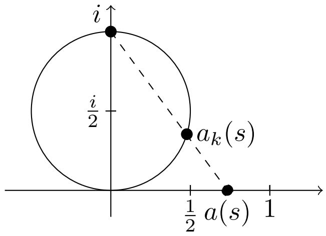

Figure 2.7: Schematic diagram of the k matrix method and the Argand circle. $a(s)$ is projected onto the Argand circle resulting in point $a_k(s)$. Since all point on the Argand circle obey the unitarity criterion these projections are unitarized.

Chapter 3

Experiment

3.1 The Large Hadron Collider (LHC)

The Large Hadron Collider (LHC) [14] is a huge circular proton-proton[1] collider at the European Organisation for Nuclear Research (CERN) designed to explore high energy physics and to help answering open questions concerning the Standard Model, in particular to find the origin of EWSB. It was built in the tunnel of the Large Electron-Positron Collider (LEP) which is situated about 100 m under the ground near Geneva, Switzerland, and has a circumference of about 27 km (see figure 3.1).

Bunches consisting of up to $1.15 \cdot 10^{11}$ protons are accelerated by more than 9000 superconducting magnets to be measured in four main detectors. First events were collected in March 2009 and from March 2010 till the end of 2011 the LHC ran with a center of mass energy of $\sqrt{s} = 7\,\text{TeV}$ and provided about $5\,\text{fb}^{-1}$ of integrated luminosity. By now LHC is running since March 2012 with a center of mass energy of $\sqrt{s} = 8\,\text{TeV}$ and it is planned to raise $\sqrt{s}$ to a maximum of 14 TeV by the end of 2014, which is the design energy for proton-proton collisions at the LHC. In November 2012 the two General Purpose Detectors *A Toroidal LHC ApparatuS* (ATLAS) and *Compact Muon Solenoid* (CMS) had collected an integrated luminosity of $20\,\text{fb}^{-1}$ each in this year, so the amount of data quadrupled in comparison to 2011 [16].

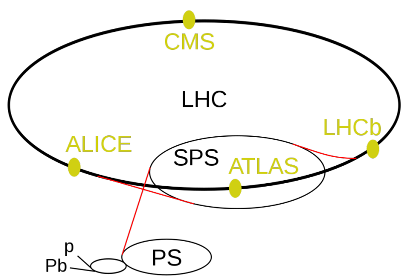

Figure 3.1: Schematical overview of the LHC. Graphic is taken from [15].

3.2 The ATLAS detector

A Toroidal LHC ApparatuS (ATLAS) [17] is one of the two general purpose detectors at the LHC (see figure 3.2). It has a cylindrical shape with a length of about 44 m and a diameter of 25 m. The detection of particles is realized in three main components, the Inner Tracker, the Calorimeters and the Muon Spectrometer.

There is a well-defined coordinate system to describe processes consistently. It is a right-handed Cartesian coordinate system, where x points to the middle of the LHC, y points vertically upwards and z points into the beam's direction. As usual ϕ measures the angle from the x axis in the x-y plane in mathematical positive direction and θ gives the angle to the z axis. Not being invariant under Lorentz transformation θ is rarely used. The

[1] It is also possible to collide heavy ions.

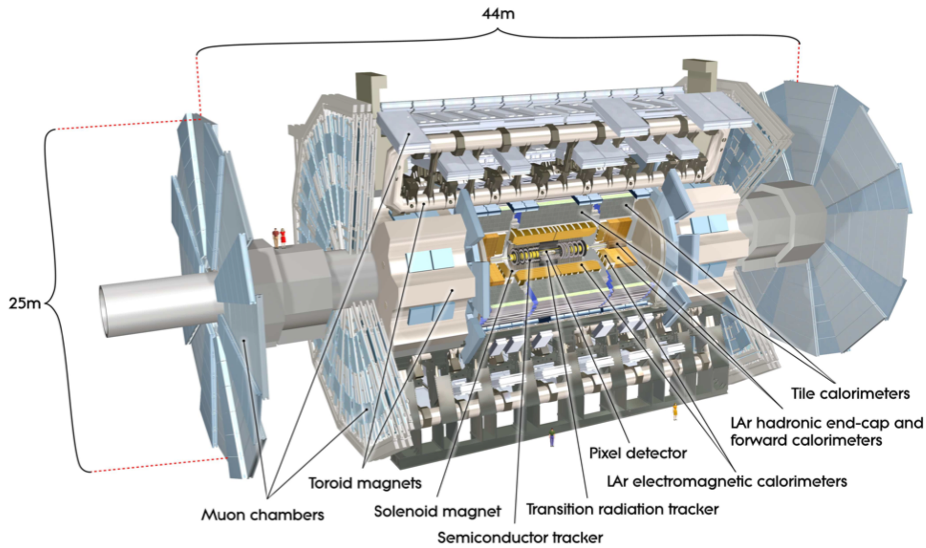

Figure 3.2: Schematic overview of the ATLAS detector. Graphic is taken from [17].

pseudorapidity η on the other hand is invariant and is defined as

$$\eta = -\ln\left(\tan\frac{\theta}{2}\right) . \tag{3.1}$$

Because the z component of the momentum is not well defined due to the not well known momentum of the partons, the transverse momentum p_{T}[2] is often used in analyses instead of the momentum p.

3.2.1 Inner Detector

The Inner Detector (ID) is divided into three subdetectors, the Silicon Pixel Detector, the Semi-Conductor Tracker and the Transition Radiation Tracker. It covers an η range of $|\eta| < 2.5$ and is permeated by a solenoid magnetic field of 2 T. This magnetic field bends the path of charged particles so that the momentum and the charge can be measured.

The Silicon Pixel Detector is the innermost detector and has therefore the highest spatial resolution requirements. With its pixel sensors this part achieves a maximum resolution of $10\,\mu$m in the R-ϕ plane and $115\,\mu$m in beam direction and it provides up to three high precision points for each track.

The Semiconductor Tracker has a slightly smaller resolution using silicon strip detectors and typically measures up to four additional points to the track.

The Transition Radiation Tracker consists of a large number of straws filled with a mixture of Xe, CO_2 and O_2 detecting the transition radiation produced by particles. This makes it a very efficient identifier for light charged particles such as electrons.

3.2.2 Calorimeter

The Calorimeter was designed to identify and measure the energy of jets, electrons and photons. It covers an η range of $|\eta| < 4.9$ and consists of the Electromagnetic Calorimeter and the Hadronic Calorimeter.

Particles interacting electromagnetically, e. g. through particle showers are most of the cases stopped in the Electromagnetic Calorimeter, so that their energy gets absorbed by lead plates and then detected by liquid argon. Hadrons on the other hand react through inelastic scattering in the Hadronic Calorimeter. Steel is used as absorber and the detector is made up

[2] defined in the x-y plane.

of scintillators in the barrel region whereas it is liquid argon based in the end caps. The quite large $|\eta|$ acceptance is achieved by the Forward Calorimeter covering the forward regions.

3.2.3 Muon spectrometer

Since muons cannot be stopped in the spectrometer, they can not be measured in the calorimeter, therefore the Muon Spectrometer was built. It covers the region $|\eta| < 2.7$ and contains the Monitored Drift Tubes (MDT), Cathode Strip Chambers (CSC), Resistive Plate Chambers (RPC) and Thin Gap Chambers (TGC). The first two are used for measuring the transverse momentum of the muons while the latter two are used for triggering as well.

3.2.4 Trigger system

The ATLAS detector measures events with a rate of 40 MHz whereas the maximum storage capability is 200 Hz. Therefore events have to be preselected by the Trigger System. This is done in three steps. The first one is the hardware based Level 1 Trigger which reduces the rate to 75 kHz with a latency of 2.5 μs. The Level 2 Trigger is software based and uses more complex algorithms and reduces the rate even further to 3.5 kHz with a latency of 40 ms. The third step is the software based Event Filter that determines more detailed information in special regions of interest. After rate is reduced to 200 Hz the events passing the Trigger System can be stored for analysis.

Chapter 4

Data simulation

All events passing the Trigger System are reconstructed later on. Therefore special algorithms try to reconstruct tracks from the hits in the detectors. The output is afterwards summarized to the AOD (*Analysis Object Data*) format containing the necessary information for later analyses.

To compare predictions of the theory with the experimental data one has to generate events following rules implied by theory. This process can be divided into several important steps. At first one has to generate so called generator or truth level events, containing the processes of the elementary particles. This is done via Monte-Carlo generators as explained in the following section. Since the LHC is a hadron collider a parton density function (PDF) is used to estimate the initial four momentum of the interacting quarks and gluons. The decay of unstable particles, hadronization, showering, initial state radiation and final state radiation have to be considered. The output can be stored in a format such as HepMC [18], which is used in this thesis, containing information about all interacting particles.

So far no detector effects have been considered. If one could build a perfect detector measuring all information of every particle exactly this would be the measured information. Since this is not possible detector effects have to be simulated in two steps. The first step simulates all interactions of the particles with the different detectors. The second step, the digitalization creates the same output format as done for data taken by the detectors. These simulated events can be treated exactly like real measured data in terms of reconstruction. This detector simulation is a very CPU-intensive process taking about 15 minutes per CPU and event.

In this thesis only truth level events without hadronization and showering are used and one aim is to compare two different Monte-Carlo generators using different aQGC models.

4.1 Monte-Carlo generators

Monte-Carlo generators are necessary for the first steps in the process of sample generation.

To simulate an event, a generator has to find possible Feynman diagrams, these can be hard-coded in databases, or dynamically generated. Then the generator has to determine the matrix element using the Feynman rules. By integrating the matrix element over the phase space using the Monte Carlo method, the generator calculates the cross sections. This means the integration is done numerically by summing over a large number of random points instead of evaluating every single point.

4.1.1 VBFNLO

VBFNLO [19] is a Monte-Carlo generator with NLO[1] QCD accuracy specialized on vector boson fusion as well as double and triple vector boson production. Using the HepMC output

[1]Next to leading order – this means that QCD loops in feynman graphs are allowed.

format as in this thesis only leading order processes can be generated. Since VBFNLO is specialized on these processes, the feynman diagrams are stored in a hard-coded database.

In addition to the Standard Model several extensions like Minimal Supersymmetric Standard Model (MSSM) and anomalous quartic gauge couplings with the parameters[2] f_0 and f_1 (see section 2.3) are available. For unitarization the form factor method is implemented. There are several other parameters available. The most important are the parton density function (pdf) or scale factors.

In this thesis three models were generated:

- The Standard Model – including a light Higgs boson
- The Standard Model extended by aQGC – parametrized by f_0 and f_1, including a light Higgs boson, without unitarization
- The Standard Model extended by aQGC – parametrized by f_0 and f_1, including a light Higgs boson, with unitarization by a form factor given by

$$\mathcal{F} = \left(1 + \frac{m(WW)^2}{\Lambda_{\mathrm{FF}}^2}\right)^{-n} \tag{4.1}$$

The parameter[3] Λ_{FF} was chosen to be small enough to unitarize all generated cases and used in all these samples. Therefore for one parameter it is expected to be smaller than necessary, implying a stronger suppression for this parameter. Since Λ_{FF} is also the same for `WWss` and `WZ` channel, this is expected to have an according influence on the `WZ` channel, too.

4.1.2 WHIZARD

WHIZARD [20] is an universal leading order Monte-Carlo generator able to compute tree-level matrix elements generating partonic event samples. Parton showering can be done directly using WHIZARD, while showering and hadronization can also be done using external tools. As in VBFNLO, beside the Standard Model alternative models, as the MSSM or anomalous quartic gauge couplings using the parameters α_4 and α_5, are available. Unitarization is done using the k matrix approach.

If aQGC are used in this model, the EWSB is realized by a Σ field. However in the used samples a light Higgs boson is also included.

- The Standard Model – including a light Higgs boson
- The Standard Model extended by aQGC – parametrized by α_4 and α_5, including a light Higgs boson, without unitarization
- Extended model – effective chiral Lagrangian, Σ field for EWSB, including a light Higgs boson, aQGC parametrized by α_4 and α_5 with k matrix unitarization

4.2 Used samples

In this thesis samples for proton-proton collisions in different channels with a center of mass energy of $\sqrt{s} = 8\,\mathrm{TeV}$ were generated with VBFNLO and WHIZARD. For analysis the Standard Model and unitarized samples with different anomalous quartic gauge couplings were generated. All samples are generated with a light Higgs boson with a mass of 126 GeV. Only one aQGC parameter at a time was set to a non-zero value, so that at least one of the two used parameters is always set to the SM value. To apply equation (2.26) the parameters f_i were chosen to be equivalent to the used α_{i+4} value. The most important parameters are listed in table 4.1.

[2] In VBFNLO these parameters are called fs_0 and fs_1.

[3] At the time of writing there was no tool for calculating the maximum Λ_{FF} available. However the authors of VBFNLO planned to publish such a tool. Therefore the authors told us the appropriate values.

As described in section 2.2 the generated final states are:

$$\texttt{WWss}: \quad jje^+\nu_e e^+\nu_e\,, \qquad\qquad \texttt{WZ}: \quad jje^+e^-e^+\nu_e\,. \tag{4.2}$$

For the same sign WW (`WWss`) channel non-unitarized samples were also generated for further comparisons.

In the following the cuts implemented in the analysis tool for the `WWss` channel are shown. For an explanation of the variables see appendix A:

$$p_T(\ell_1) > 25\,\text{GeV} \qquad p_T(j_1) > 30\,\text{GeV} \tag{4.3}$$
$$p_T(\ell_2) > 20\,\text{GeV} \qquad p_T(j_2) > 30\,\text{GeV} \tag{4.4}$$
$$|\eta(\ell)| \in [0, 1.37] \cup [1.52, 2.47] \qquad |\eta(j)| < 5 \tag{4.5}$$
$$m(\ell\ell) > 20\,\text{GeV} \qquad m(jj) > 500\,\text{GeV} \tag{4.6}$$
$$\zeta > -0.5 \qquad |\eta_{jj}| > 2.4 \tag{4.7}$$
$$E_{\mathrm{T}}^{\mathrm{miss}} > 40\,\text{GeV}\,. \tag{4.8}$$

In the `WZ` channel the following cuts were used:

$$p_{\mathrm{T}}(\ell_1) > 25\,\text{GeV} \qquad p_{\mathrm{T}}(j) > 30\,\text{GeV} \tag{4.9}$$
$$p_{\mathrm{T}}(\ell_2) > 20\,\text{GeV} \tag{4.10}$$
$$p_{\mathrm{T}}(\ell_3) > 20\,\text{GeV} \tag{4.11}$$
$$|\eta(\ell)| \in [0, 1.37] \cup [1.52, 2.47] \qquad |\eta(j)| < 5 \tag{4.12}$$
$$m(\ell^+\ell^-) > 10\,\text{GeV} \qquad m(jj) > 500\,\text{GeV} \tag{4.13}$$
$$\zeta > -0.5 \qquad |\eta_{jj}| > 2.4 \tag{4.14}$$
$$E_{\mathrm{T}}^{\mathrm{miss}} > 40\,\text{GeV}\,. \tag{4.15}$$

parameter	value
center of mass energy $\sqrt{s}$	8 TeV
Higgs mass	126 GeV
Higgs width	0.00418 GeV
Top mass	172.5 GeV
τ mass	1.77705 GeV
scale μ_F	160.798 GeV
scale μ_R	160.798 GeV
Fermi Constant G_F	$1.16639 \cdot 10^{-5}\,\text{GeV}^{-2}$
$W^\pm$ mass	80.399 GeV
Z mass	91.1876 GeV
Parton distribution function (PDF)	`cteq6ll.LHpdf`

Table 4.1: List of most important parameters with chosen values for the generation. To calculate other parameters the GF scheme was used.

Chapter 5

Validity check

There are several possibilities to validate the results and the generation of events. This is important to make sure the different generators and models are consistent and to avoid errors in event generation.

5.1 Total cross section of the SM process

A simple possibility is to check if all approaches have the same result in the SM case. Both generators have a special mode for the SM process. However all other modes should reproduce the SM result if all parameters are set to SM values. This means for both generators that aQGC can be turned on, but chosen to be equal to zero. Additionally the unitarization can be used. In a first step the total cross sections should be equal. These can be found in table 5.1.

All values for the `WWss` channel are in a good agreement. In VBFNLO with aQGC = 0 the unitarization has no effect. But since the form factor only effects the modifications of the aQGC (see chapter 6), this is plausible. In the `WZ` channel there is a difference between the two generators. The `WZ` samples also include a $W^+\gamma^*$[1] channel. This leads to a raise of the cross section for low invariant masses of the leptons coming from the γ^*. Therefore in the VBFNLO samples a cut is included in the generators to simulate only events, where all combinations of opposite-charged leptons have an invariant mass of $m(l^+l^-) \geq 4\,\mathrm{GeV}$. This cut was not included in the WHIZARD samples, leading to too high total cross sections. This has no effect on the shapes of the further analyses since this cut was included in the analysis using the RIVET [21] tool. New samples that include this cut were generated, but it was not enough time to use only these new samples. Therefore the total cross section of the SM process is listed in addition to the older samples to estimate the influences of this effect. Since σ is compatible with the results of the VBFNLO samples this missing cut is expected to be the reason for the discrepancies.

5.2 Differential cross section of the SM process

A next possibility to check the validity is to compare the differential cross sections of these SM samples. The most important distributions are shown in figure 5.1 for the `WWss` channel and in figure 5.2 for the `WZ` channel.

Besides the large statistical uncertainty especially in the `WZ` samples generated with WHIZARD these distributions show a very good agreement. The VBFNLO samples were generated weighted. This could be a reason for the smaller statistical uncertainties than in the unweighted WHIZARD samples. All in all these samples are consistent with each other and with the knowledge of the missing cut and its effects one can use these samples for further analyses.

[1] γ^* takes place of the Z^0 in the relevant diagrams.

		$\sigma_{\mathtt{WWss}}$ [fb]	$\sigma_{\mathtt{WZ}}$ [fb]
VBFNLO	without aQGC	0.6534 ± 0.0026	0.3007 ± 0.0035
	with aQGC $= 0$, non-uni	0.6534 ± 0.0026	0.2998 ± 0.0035
	with aQGC $= 0$, uni	0.6534 ± 0.0026	0.2998 ± 0.0035
WHIZARD	without aQGC	0.6606 ± 0.0012	0.3211 ± 0.0020
	with aQGC $= 0$, non-uni	0.641 ± 0.011	not generated
	with aQGC $= 0$, uni	0.6593 ± 0.0012	0.3425 ± 0.0028
	without aQGC, with cut		0.3037 ± 0.0013

Table 5.1: Total cross sections of the SM process for all different generation methods. “without aQGC” represents the SM process. All samples labeled with “with aQGC = 0” are generated using the SM extended by aQGC, with all parameters set to SM values. “uni” – unitarized. “non-uni” – non-unitarized. For the `WZ` channel no non-unitarized samples have been generated using WHIZARD. In the last line an additional generated sample is shown, which includes a $m(l^+l^-) \geq 4\,\mathrm{GeV}$ cut in the `WZ` channel, which was missing in the other WHIZARD samples. This shows, that the observed discrepancies seemed to be caused by this missing cut. Uncertainties are given by generator.

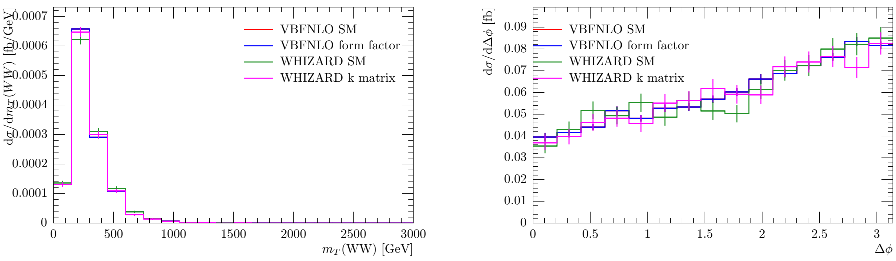

Figure 5.1: Comparison of different models for the `WWss` SM process. The left distribution shows the differential cross section over the transverse mass of the pair of vector bosons $m_{\mathrm{T}}(WW)$. The right distribution shows the differential cross section dependency on the absolute value of the angle between the projections of the leptons’ momenta in the x-y plane $\Delta\phi(ll)$. The red and green lines show the distributions of the SM process generated by VBFNLO or WHIZARD respectively. The blue and magenta distributions are generated using the SM extended with aQGC (SM values) by VBFNLO or WHIZARD respectively.

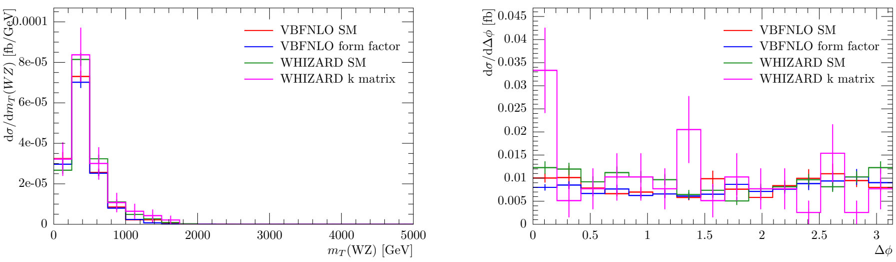

Figure 5.2: Comparison of different models for the `WZ` SM process. The left distribution shows the differential cross section over the transverse mass of the pair of vector bosons $m_{\mathrm{T}}(WZ)$. The right distribution shows the differential cross section dependency on the absolute value of the angle between the projections of the vector bosons’ momenta in the x-y plane $\Delta\phi(WZ)$. The red and green lines show the distributions of the SM process generated by VBFNLO or WHIZARD respectively. The blue and magenta distributions are generated using the SM extended with aQGC (SM values) by VBFNLO or WHIZARD respectively.

Chapter 6

Total cross sections

The first step is to study the total cross section's dependency on anomalous quartic gauge couplings. If this is understood, it is possible to set limits on the aQGC parameters once the total cross section is measured.

6.1 Dependency on aQGC

The additional terms in the effective Lagrangian lead to new terms in the matrix element M. Those new terms depend on the aQGC parameters and since the total cross section σ can be calculated using the matrix element, σ also depends on the aQGC parameter. Using the aQGC parameter α this can be expressed by the matrix element $M \equiv \alpha \cdot M_{\text{aQGC}} + M_{\text{SM}}$ which leads to

$$\begin{aligned}
\mathrm{d}\sigma &= |M|^2 \,\mathrm{d}\Phi \\
\sigma &= \int \alpha^2 \left|M_{\text{aQGC}}\right|^2 + 2\alpha \underbrace{\left(\mathrm{Re}(M_{\text{aQGC}})\,\mathrm{Re}(M_{\text{SM}}) + \mathrm{Im}(M_{\text{aQGC}})\,\mathrm{Im}(M_{\text{SM}})\right)}_{\equiv M_{\text{Interference}}} + \left|M_{\text{SM}}\right|^2 \mathrm{d}\Phi \\
&= \alpha^2 \underbrace{\int \left|M_{\text{aQGC}}\right|^2 \,\mathrm{d}\Phi}_{\equiv \sigma_{\text{aQGC}}} + \alpha \cdot \underbrace{2 \int \left|M_{\text{Interference}}\right| \,\mathrm{d}\Phi}_{\equiv \sigma_{\text{Int}}} + \underbrace{\int \left|M_{\text{SM}}\right|^2 \,\mathrm{d}\Phi}_{\equiv \sigma_{\text{SM}}} \\
&\equiv \alpha^2 \cdot \sigma_{\text{aQGC}} + \alpha \cdot \sigma_{\text{Int}} + \sigma_{\text{SM}} \,.
\end{aligned} \tag{6.1}$$

This can be done for f in an analog way leading to different values for σ_{aQGC} and σ_{Int}. This implies a parabolic dependency of the cross section σ on the aQGC parameters α and f respectively. This is shown in figure 6.1 for f_0 in the `WWss` channel. The non-unitarized samples are in a good agreement with a parabolic fit. Comparing all distributions one can see that the parabolic fits for f_0 and f_1 are nearly identical. However the WHIZARD samples have the same cross section when α_4 is the half of α_5. For the `WZ` channel non-unitarized samples were generated only with VBFNLO. These distributions show a difference between f_0 and f_1, while $f_0 \approx \frac{2}{3} f_1$ applies for any given cross section. Another important thing to notice is that the minimum of the fits is always close to the SM case. This implies that σ_{Int} is small compared to σ_{aQGC}. Therefore cross sections of positive and negative aQGC parameters are similar.

6.2 Effects of unitarization

The right distribution in figure 6.1 shows the dependence of σ on f_0 for the unitarized samples. The cross sections do not agree well with the parabolic fit. The effect of the unitarization gets more important with larger absolute values of aQGC. Therefore cross sections of high aQGC parameters are suppressed while cross sections near to the SM case are not influenced much.

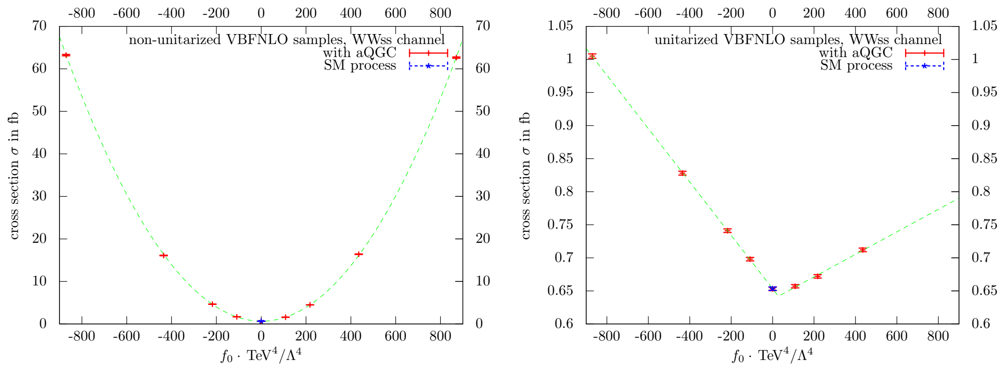

Figure 6.1: Dependency of σ on the aQGC parameter f_0 for the WWss channel. Left: non-unitarized samples. Right: unitarized samples. Red crosses correspond to the cross sections of the generated samples. Blue data points refer to the cross section of the samples generated using the mode for the SM process. The green dashed line is a parabolic fit for non-unitarized samples. For the unitarized samples it is a combination of two linear fits with independet slopes for different values for the aQGC parameter. Other channels and parameters can be found in appendix C.1

		σ_{aQGC} [fb]	σ_{Int} [fb]	σ_{SM} [fb]
VBFNLO	f_0, WWss	$(8.23 \pm 0.03) \cdot 10^{-5}$	$(-2.8 \pm 1.0) \cdot 10^{-4}$	0.654 ± 0.007
	f_1, WWss	$(8.23 \pm 0.01) \cdot 10^{-5}$	$(-3.5 \pm 0.4) \cdot 10^{-4}$	0.654 ± 0.002
	f_0, WZ	$(7.47 \pm 0.03) \cdot 10^{-6}$	$(-2.8 \pm 0.9) \cdot 10^{-5}$	0.298 ± 0.002
	f_1, WZ	$(3.31 \pm 0.01) \cdot 10^{-6}$	$(-2.4 \pm 0.4) \cdot 10^{-5}$	0.301 ± 0.002
WHIZARD	α_4, WWss	656 ± 21	-0.9 ± 1.7	0.63 ± 0.02
	α_5, WWss	183 ± 10	-1.70 ± 1.5	0.64 ± 0.04

Table 6.1: Table including the fit parameters σ_{aQGC}, σ_{SM} and σ_{SM} for the dependency of σ on the aQGC parameters corresponding to equation (6.1). The second column lists the varied couping parameter and the channel. The parameter not listed has the SM value. Note that the value of the fit parameters σ_{aQGC} and σ_{SM} depends on the aQGC parametrization and therefore is not comparable for different generators.

So the expected dependency would be nearly parabolic for aQGC close to the SM process with growing differences for larger absolute values of aQGC. In most of the channels these cross sections are better represented by seperated linear fits. Therefore a threshold value was fitted as cross section of two simultaneously fitted linear functions. The similarity for positive and negative aQGC values is not given any more, which indicates a larger influence of the interference term. The minimum of the cross section curve, as well as the threshold value, is therefore shifted to positive values of the aQGC parameter. This could be caused by the phase space dependent suppression of the unitarization methods. A point to be studied are the differences between α_4 and α_5 or f_0 and f_1 respectively, since the domination of the interference term seems to differ between the two parametrizations. The use of the same Λ_{FF} for both, f_0 and f_1, in the form factor method is expected to be a reason for that.

Comparing the distributions for the other channels one can see, that the unitarized cross sections are much smaller than the non-unitarized cross sections. Especially the form factor approach strongly suppresses the differences to the SM. Thus in the WZ channel there is hardly any difference to be seen after the form factor unitarization.

In table 6.1 there is a list of all fit parameters for a parabolic fit[1]. These numbers are consistent with the observations given above. For all non-unitarized samples, the influence of σ_{Int} is smaller than the influence of σ_{aQGC}. In the region of the generated samples the influence is smaller by a factor in the order of 10^{-2}.

[1]Not plotted for the unitarized samples.

Chapter 7

Differential cross sections

Once the total cross sections are understood, a further possibility for analyses is the study of the differential cross sections. The shapes of the differential cross sections provide a good possibility to tighten the limits on the anomalous quartic gauge couplings and to study the influences of the different coupling parameters.

7.1 Discriminating observables

The first step of this analysis is to find discriminating observables which show a dependency on the coupling parameters. Therefore samples with rising values for the aQGC parameters were generated using WHIZARD and VBFNLO. These samples are now analyzed with RIVET to create distributions for a couple of observables. Larger absolute values of the aQGC parameter should lead to larger total cross section. This is not always the case for positive aQGC parameters due to the different influence of the interference term (see appendix C.1). Thus negative values of the aQGC parameters are used in this study to have a more consistent result. A selection of the resulting distributions for all different channels and aQGC parameters can be found in appendix C.2. Comparing these one sees some discriminating observables, most notably the transverse invariant mass of the pair of gauge bosons $m_T(WW)$ or $m_T(WZ)$ respectively and the angle in the transverse plane between the leptons $\Delta\phi(\ell\ell)$ or between the boson pair $\Delta\phi(WZ)$ respectively. The transverse mass is used, because the invariant mass of the boson pair cannot be reconstructed for the WW case. This is because the momentum of the neutrinos in the event cannot be fully reconstructed by the measured missing transverse energy estimated using momentum conservation in the detector. The transverse mass is therefore calculated with this missing transverse energy $E_{\mathrm{T}}^{\mathrm{miss}}$ using the equation $m_{\mathrm{T}} = p_\mu p^\mu$ and

$$p^\mu = p(\ell_1)^\mu\Big|_{p_z=0} + p(\ell_2)^\mu\Big|_{p_z=0} + \begin{pmatrix} E_{\mathrm{T}}^{\mathrm{miss}} \\ -p_{\mathrm{sum},\,x} \\ -p_{\mathrm{sum},\,y} \\ 0 \end{pmatrix} \tag{7.1}$$

with the vectorial sum of all measured momenta p_{sum}.

There are also other discriminating observables with less significant effects, e. g. the kinematics of the jets. $|\eta|$ and p_{T} of both leptons or the invariant mass of both jets m_{jj} do not only scale with the cross section, but also vary their shape. On the other hand the remaining kinematics of the leptons do only scale with the cross section, leading to a constant ratio to the SM process. Besides the already mentioned $\Delta\phi(\ell\ell)$, especially the lepton centrality ζ and the invariant mass of the leptons $m_{\ell\ell}$ show differences compared to the shape of the SM process.

7.2 Effects of aQGC on observables

Figure 7.1 shows the distributions of the most discriminating observables for the `WWss` channel and the aQGC parameter f_0, other observables are shown in appendix C.2. There are large differences to be seen in most of the distributions. The strongly rising total cross section can be seen, since the distributions are scaled with respect to the cross section. Thus the curve of the SM process in figure 7.1 is barely visible. These distributions show, that additional events through the aQGC have a large $m_{\mathrm{T}}(WW)$ and a $\Delta\phi(\ell\ell)$ close to π. This indicates that the leptons are going in opposite directions. Thus also the gauge bosons are back to back. The distributions for the WHIZARD samples show a good agreement, besides the different scaling, to the shapes of the VBFNLO distributions. An interesting thing to notice is that the shapes for same values of f_0 and f_1 are not distinguishable within statistical uncertainty, while for α_i this is realized for $\alpha_4 \approx 2 \cdot \alpha_5$. This corresponds to the results seen in chapter 6.1. The differences can also be seen for the WZ channel. The distributions of $\Delta\phi(WZ)$ correspond to the $\Delta\phi(\ell\ell)$ which implies a similar shape as it can be seen in appendix C.2.

The steep rise in $m_{\mathrm{T}}(WW)$ or $m_{\mathrm{T}}(WZ)$ respectively could be caused by a divergence of the cross section (see section 2.4), since no unitarization is applied and therefore unitarity can not be guaranteed. In these samples it is suppressed by the parton density function (PDF). These samples are expected to be not physical and therefore not measurable.

7.3 Effects of unitarization

In figure 7.2 the corresponding distributions to figure 7.1 with unitarization are shown. Since the additional terms in the matrix element are suppressed, the resulting shapes are similar to the SM process. Due to the dependency of the form factor unitarization on $\sqrt{s}$, the shape gets closer to the shape of the SM process with rising $m_{\mathrm{T}}(WW)$. The peak in the $\Delta\phi_{\ell\ell}$ distribution is less significant. For the used values for f_0 and f_1, $\Delta\phi(\ell\ell)$ is the only significantly discriminating observable. Along with that, jet kinematics and the $m_{\mathrm{T}}(WW)$ do vary their shape compared to the SM process. Thereby, also for the `WZ` channel, f_1 is closer to the SM process than the shapes of the f_0 samples, so the form factor unitarization has different effects on the different aQGC parameters.

For the WHIZARD samples $m_{\mathrm{T}}(WW)$ and the kinematic distributions of the jets do separate more significantly the aQGC from the SM process. Unlike the form factor samples, the samples using the k Matrix do not agree with the SM process for large $m_{\mathrm{T}}(WW)$. However they agree with each other with a shift to the SM.

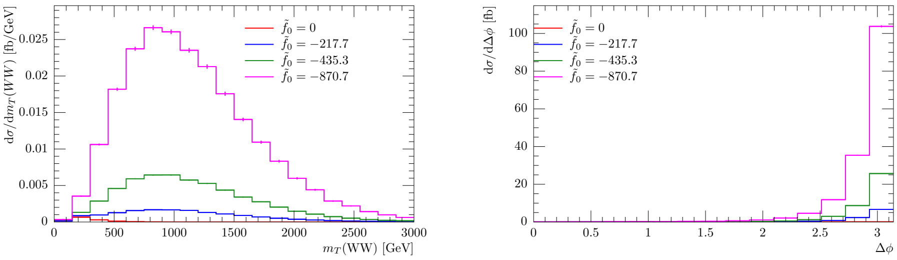

Figure 7.1: Comparison of different values for aQGC parameter f_0, with $f_1 = 0$, in the `WWss` channel. No unitarization was used. The left distribution shows the differential cross section over the transverse mass $m_\mathrm{T}(WW)$. The right distribution shows the differential cross section dependency on the absolute value of the angle between the projections of the leptons' momenta in the x-y plane $\Delta\phi(ll)$. The different colors represent different values for $\tilde{f}_0$ as listed in the key.

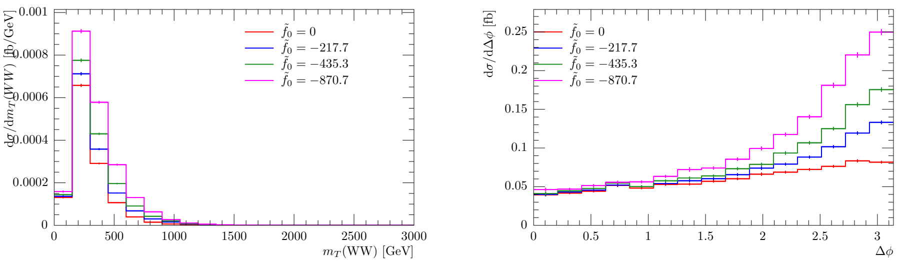

Figure 7.2: Comparison of different values for aQGC parameter f_0 in the `WWss` channel. For unitarization a form factor was applied. The left distribution shows the differential cross section over the transverse mass $m_\mathrm{T}(WW)$. The right distribution shows the differential cross section dependency on the absolute value of the angle between the projections of the leptons' momenta in the x-y plane $\Delta\phi(ll)$. The different colors represent different values for $\tilde{f}_0$ as listed in the key.

Chapter 8

Conversion between different aQGC parametrizations

Theory predicts a relationship between f_i and α_{i+4} as described in section 2.3. It was tried to find a factor for an assumed linear proportionality. Thereby it was tested whether f_i and α_{i+4} are related in this way or not.

8.1 Comparison of non-unitarized samples

The first step was to match the parabolic fits of the total cross sections by varying the scale. The results are shown in figure 8.1. Since no WHIZARD samples without unitarization were generated for the `WZ` channel, the following part only applies to the `WWss` channel. For these distributions the cross sections for both parameters were fitted in the same parabola with an additional fitting parameter, the scale $t_i = \frac{f_i}{\alpha_{i+4}}$. This is also used as scale between the different x axes. This results in a combined distribution with one variable and one fixed x axis. Since the distributions for non-unitarized samples agree very well with their parabolic fit, the agreement with the combined fit is good. The resulting parameters t_i are listed in table 8.1. This is consistent with the results from chapter 6 since for a given cross section, f_0 equals f_1 and α_4 is the half of α_5. But these scaling factors are neither equal to each other nor to the predicted value. One important thing to be studied in further analyses are the discrepancies between the predicted values and the results from the generated samples. For some reason the predicted value is the mean of the calculated factors.

		$t_i = f_i/\alpha_{i+4}$
predicted (see equation (2.26))		$\frac{8\Lambda^4}{g^2 v^4} \approx 2176$
non-unitarized	`WWss` for f_0 and α_4	2815.63 ± 53.46
	`WWss` for f_1 and α_5	1485.48 ± 27.58
unitarized	`WWss` for f_0 and α_4	$(1.50 \pm 0.18) \cdot 10^4$
	`WWss` for f_1 and α_5	$(5.6 \pm 3.8) \cdot 10^4$
	`WZ` for f_0 and α_4	$(2.50 \pm 0.13) \cdot 10^4$
	`WZ` for f_1 and α_5	$(6.0 \pm 5.9) \cdot 10^4$

Table 8.1: List of the fit parameters t_i. The second column lists the corresponding channel and the varied and compared parameters, parameters not listed have their SM value. Second and third line show values for unitarized samples, while in lines five to seven values for unitarized samples are listed. Non-unitarized samples were fitted in a parabolic fit. Unitarized samples were fitted according to equation (8.1).

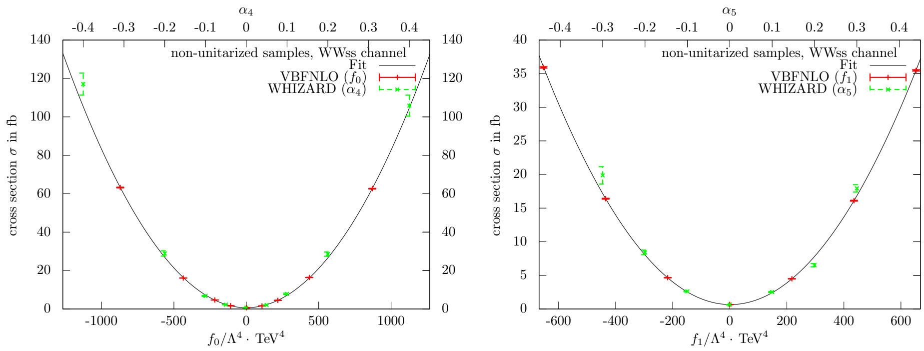

Figure 8.1: Dependency of σ on the aQGC parameter f_i and α_{i+4} for the `WWss` channel, non-unitarized samples. Left: parameters f_0 and α_4. Right: parameters f_1 and α_5. Red crosses correspond to the cross sections of the samples generated by VBFNLO. Green data points refer to the cross section of the samples generated by WHIZARD. The black line is a parabolic fit for all samples. f_i-axis was scaled to match α_{i+4}-axis according to fit parameter t_i. Other channels and parameters can be found in appendix C.3.

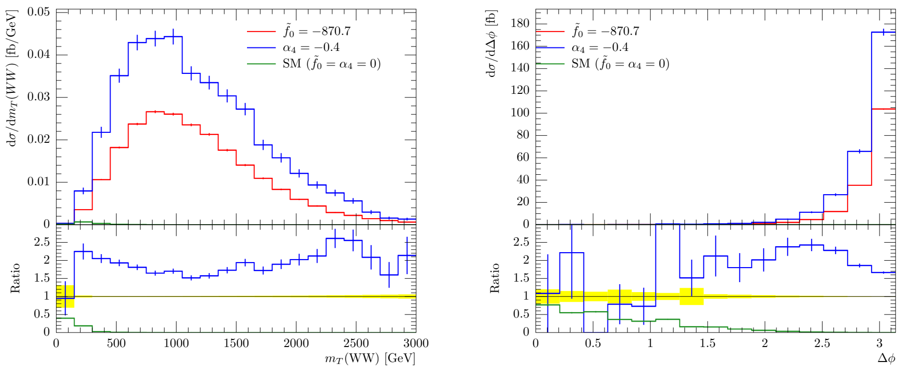

Figure 8.2: Comparison of values for aQGC parameter f_0 and α_4, that are predicted to match, with $f_1 = \alpha_5 = 0$, in the `WWss` channel. No unitarization was used. The left distribution shows the differential cross section over $m_{\mathrm{T}}(WW)$. The right distribution shows the differential cross section dependency on the absolute value of the angle between the projections of the leptons' momenta in the x-y plane $\Delta\phi(\ell\ell)$. In the ratio plot the ratio to the distribution with $\tilde{f}_0 = -870.7$ is given.

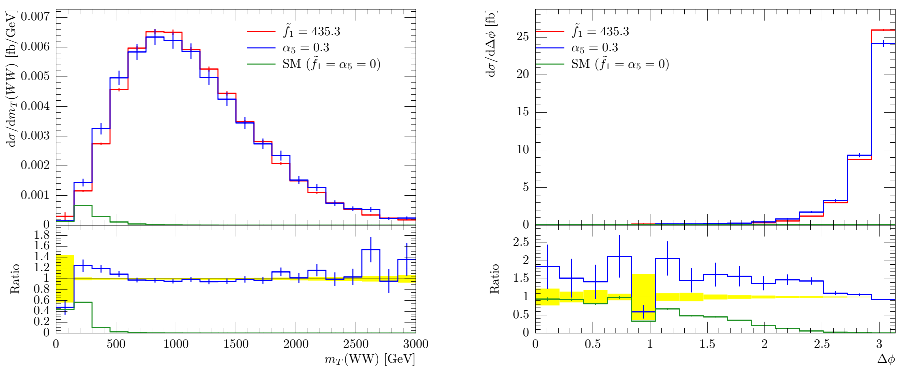

Figure 8.3: Comparison of values for aQGC parameter f_1 and α_5, with similar cross section, with $f_0 = \alpha_4 = 0$, in the `WWss` channel. No unitarization was used. The left distribution shows the differential cross section over $m_{\mathrm{T}}(WW)$. The right distribution shows the differential cross section dependency on the absolute value of the angle between the projections of the leptons' momenta in the x-y plane $\Delta\phi(\ell\ell)$. In the ratio plot the ratio to the distribution with $\tilde{f}_1 = -435.3$ is given.

A further check in figure 8.2 a pair of parameters is shown, that is predicted in equation (2.26) to have the same results. These show significant differences not only in the total cross section, but also in the shape of the distributions. So these samples are not consistent to each other. On the other hand the samples in figure 8.3 are in a good agreement. These are samples with a similar cross section, and therefore are close to the scaling factor given in table 8.1 calculated using the fit in one combined parabola.

8.2 Comparison of unitarized samples

Since unitarity cannot be ensured the generated samples are assumed to be not physical. For comparison with data one has to use unitarized samples. Therefore it is important to study the influences of unitarity on the conversion between f_i and α_{i+4}.

As explained in section 6.2 unitarity breaks the parabolic dependency on the aQGC parameter. Thus another fit was used to compare the samples of f_i and α_{i+4}. Since the form factor approach suppresses the total cross sections stronger than the k matrix approach does, only a smaller α_i range was studied, ignoring the samples with $|\alpha_i| = 0.4$. In this range the total cross sections can be estimated in a linear fit using different slopes for positive and negative values for the aQGC. The interference term has more influence and therefore the minimum of σ is not at $f_i = 0$ or $\alpha_{i+4} = 0$ respectively (see section 6.2). Therefore one could increase the agreement of the fit by varying the point where the slope changes to a larger value. For simplicity's sake this was not done here, since the influence is not expected to be large. The cross sections for all samples of each channel were fitted using the function

$$\sigma = \begin{cases} a_i \cdot (t_i \cdot \alpha_{i+4}) + \sigma_{\mathrm{SM}} & , \alpha_{i+4} < 0 \\ b_i \cdot (t_i \cdot \alpha_{i+4}) + \sigma_{\mathrm{SM}} & , \alpha_{i+4} > 0 \\ a_i \cdot (f_i) + \sigma_{\mathrm{SM}} & , f_i < 0 \\ b_i \cdot (f_i) + \sigma_{\mathrm{SM}} & , f_i > 0 \end{cases} \tag{8.1}$$

with the fitting parameters a_i, b_i, and t_i, latter is listed in table 8.1 for all channels. The resulting distributions for the `WWss` channel are shown in figure 8.4. The x axes is adjusted to the fitted scale t_i. Comparing the scaling factors listed in table 8.1 one sees that the scaling factors are not any more in the order of magnitude of the predicted value. Since the form factor unitarization results in smaller cross sections, higher values of f_i match a given α_{i+4}. Since the differences to the SM cross section are small for f_i in the `WZ` channel the t_i are even larger than in the `WWss` channel and the fits of t_i are inaccurate. The largest simulated values for $|f_i|$ correspond to the smallest $|\alpha_{i+4}| \neq 0$ for $i = 0$ and even smaller values for $i = 1$. Thus to determine a relationship for the unitarized samples one would have to generate more samples with smaller α_{i+4} and higher f_i.

Figures 8.5 and 8.6 show a comparison of the differential cross sections for different pairs of f_i and α_{i+4}. Figure 8.5 shows a pair according to the predicted relation. These samples do not match compared to the samples shown in figure 8.6. These are in a good agreement with each other, both in shape and in cross section. However there are more differences than for non-unitarized samples. These are differences of the unitarization methods, in addition to the stronger suppression by the form factor unitarization. Since the unitarization methods depend on the invariant mass of the bosons, there is a discrepancy to be seen in these distributions. There are also differences in the p_{T} distributions of the jets and leptons. These differences can be seen in particular regions of low $|\eta|$ of the jets and in the high energy regions for jets and leptons (see appendix C.3).

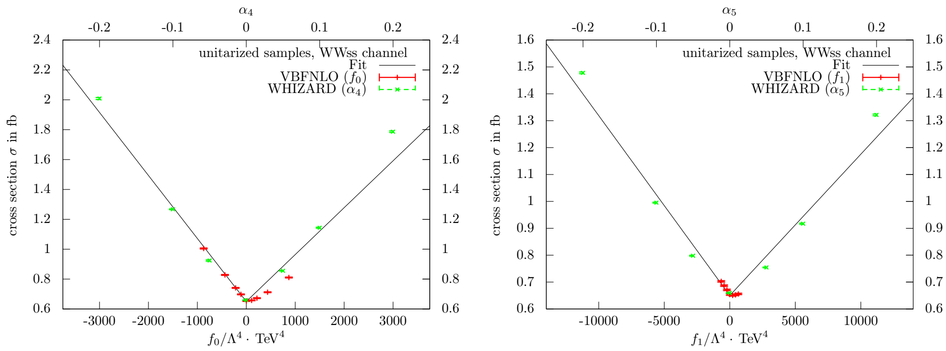

Figure 8.4: Dependency of σ on the aQGC parameter f_i and α_{i+4} for the WWss channel, unitarized samples. Left: parameters f_0 and α_4. Right: parameters f_1 and α_5. Red crosses correspond to the cross sections of the samples generated by VBFNLO. Green data points refer to the cross section of the samples generated by WHIZARD. The black line is a fit for all samples according to equation (8.1). f_i-axis was scaled to match α_{i+4}-axis according to fit parameter t_i. Other channels and parameters can be found in appendix C.3.

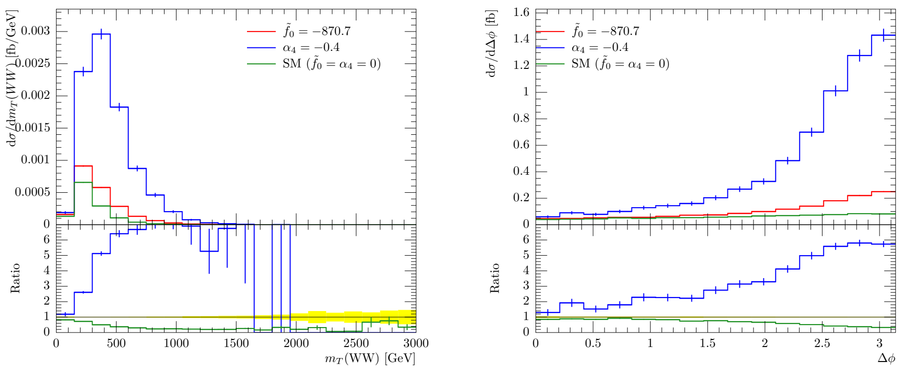

Figure 8.5: Comparison of values for aQGC parameter f_0 and α_4, that are predicted to match, with $f_1 = \alpha_5 = 0$, in the `WWss` channel. Unitarization was applied. The left distribution shows the differential cross section over $m_T(WW)$. The right distribution shows the differential cross section dependency on the absolute value of the angle between the projections of the leptons' momenta in the x-y plane $\Delta\phi(\ell\ell)$. In the ratio plot the ratio to the distribution with $\tilde{f}_0 = -870.7$ is given.

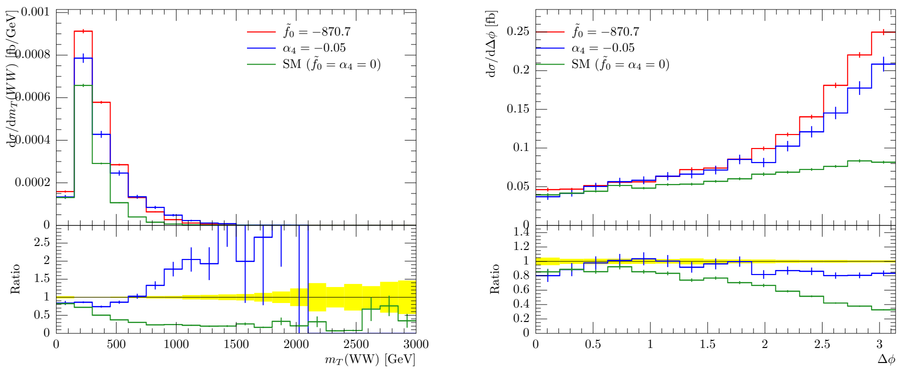

Figure 8.6: Comparison of values for aQGC parameter f_0 and α_4, with similar cross section, with $f_1 = \alpha_5 = 0$, in the `WWss` channel. Unitarization was applied. The left distribution shows the differential cross section over $m_T(WW)$. The right distribution shows the differential cross section dependency on the absolute value of the angle between the projections of the leptons' momenta in the x-y plane $\Delta\phi(\ell\ell)$. In the ratio plot the ratio to the distribution with $\tilde{f}_0 = -870.7$ is given.

Chapter 9

Summary

In this thesis the effects of different aQGC parametrizations on Vector Boson Scattering were analyzed and compared. The aim was to understand the influences and the differences between them. This is a necessary foundation for the possibility to set limits on the aQGC parameters in further analyses. For that reason Monte-Carlo samples of proton-proton collisions at $\sqrt{s} = 8\,\text{TeV}$ were analyzed on truth level.

The reproduction of the SM process for different models showed a good agreement, indicating that the generators seem to be consistent. The dependency of the total cross section on the aQGC parameters is parabolic for non-unitarized samples but differs for unitarized samples. This was expected due to the suppression of σ by the unitarization. However the predicted conversion of the different parametrizations (2.24) was neither consistent with the results of unitarized nor non-unitarized samples. The conversion, listed in table 8.1, of non-unitarized samples was in the order of magnitude of the prediction. Compared to the prediction, the results showed a different relation for f_0 and f_1. For a given cross section f_0 and f_1 were nearly identical while α_5 was about the half of α_4. This was not expected.

The comparison of unitarized samples showed that the form factor unitarization suppressed the total cross section more than the k matrix method does. There are also differences between samples, having similar total cross sections after unitarization. This shows that the choice of the unitarization method has an influence not only on the total cross section but also on the shape of the differential distributions.

These are important questions to be studied in further analyses. Especially the differences of the non-unitarized samples to the prediction have to be understood before setting limits on the aQGC parameters. For further analyses a conversion of the different parametrizations for the unitarized cases would be helpful. To determine it one would have to generate more samples. In WHIZARD the additional cut on the invariant mass of the leptons would have to be included and in VBFNLO the parameter Λ_{FF} of the unitarization should be adjusted to the different channels and parameters.

Appendix A

List of used variables

Name	Description	Formula
$\boldsymbol{\eta}$	Pseudorapidity	$\eta \equiv -\ln\left(\tan\frac{\theta}{2}\right)$
$\boldsymbol{\tilde{f}_i}$	Abbreviation for anomalous coupling parameter f_i to make it independed of energy scale Λ and to work without dimension.	$\tilde{f}_i \equiv \frac{f_i \cdot \mathrm{TeV}^4}{\Lambda^4}$
$\boldsymbol{\Lambda}$	Energy scale up to which die SM is valid.	
$\boldsymbol{\Lambda_{\mathrm{FF}}}$	Parameter of form factor unitarization. Is also an energy scale, but is independent of Λ.	
$\boldsymbol{E_{\mathrm{T}}^{\mathrm{miss}}}$	Missing transverse energy.	
$\boldsymbol{m(WW),\ m(WZ)}$	Invariant mass of the boson pair. Calculated using the mass if the leptons and neutrinos.	
$\boldsymbol{m_{\mathrm{T}}(WW),\ m_{\mathrm{T}}(WZ)}$	Transverse invariant mass of the boson pair. Calculated using the mass of visible particles.	
$\boldsymbol{m(jj)}$	Invariant mass of the jet pair	
$\boldsymbol{m(\ell\ell)}$	Invariant mass of the lepton pair	
$\boldsymbol{p_{\mathrm{T}}}$	Transverse momentum	
$\boldsymbol{\zeta}$	Lepton centrality	$\zeta_{\ell\ell} \equiv \min\left\{\min\{\eta_1^\ell,\eta_2^\ell\} - \min\{\eta_1^j,\eta_2^j\}\ ,\ \max\{\eta_1^j,\eta_2^j\} - \max\{\eta_1^\ell,\eta_2^\ell\}\right\}$

Appendix B

List of all samples

Generator	f_0	f_1	α_4	α_5	cross section σ	comment
VBFNLO	0	0			0.3007 ± 0.0035	SM with Higgs
VBFNLO	0	0			0.2998 ± 0.0035	
VBFNLO	0	0			0.2998 ± 0.0035	unitarized
VBFNLO	-870.7	0			6.0124 ± 0.0334	
VBFNLO	-435.3	0			1.7264 ± 0.0096	
VBFNLO	-217.7	0			0.6597 ± 0.0064	
VBFNLO	-108.8	0			0.3864 ± 0.0030	
VBFNLO	108.8	0			0.3889 ± 0.0038	
VBFNLO	217.7	0			0.6447 ± 0.0049	
VBFNLO	435.3	0			1.6926 ± 0.0095	
VBFNLO	870.7	0			5.9293 ± 0.0292	
VBFNLO	-870.7	0			0.3448 ± 0.0111	unitarized, $\Lambda_{\mathrm{FF}} = 543$
VBFNLO	-435.3	0			0.3180 ± 0.0043	unitarized, $\Lambda_{\mathrm{FF}} = 637$
VBFNLO	-217.7	0			0.3022 ± 0.0029	unitarized, $\Lambda_{\mathrm{FF}} = 755$
VBFNLO	-108.8	0			0.3059 ± 0.0040	unitarized, $\Lambda_{\mathrm{FF}} = 905$
VBFNLO	108.8	0			0.3113 ± 0.0082	unitarized, $\Lambda_{\mathrm{FF}} = 905$
VBFNLO	217.7	0			0.3033 ± 0.0044	unitarized, $\Lambda_{\mathrm{FF}} = 755$
VBFNLO	435.3	0			0.3097 ± 0.0033	unitarized, $\Lambda_{\mathrm{FF}} = 637$
VBFNLO	870.7	0			0.3178 ± 0.0038	unitarized, $\Lambda_{\mathrm{FF}} = 543$
VBFNLO	0	-870.7			2.8356 ± 0.0163	
VBFNLO	0	-435.3			0.9336 ± 0.0074	
VBFNLO	0	-217.7			0.4662 ± 0.0041	
VBFNLO	0	-108.8			0.3394 ± 0.0025	
VBFNLO	0	108.8			0.3357 ± 0.0026	
VBFNLO	0	217.7			0.4523 ± 0.0039	
VBFNLO	0	435.3			0.9256 ± 0.0109	
VBFNLO	0	870.7			2.7893 ± 0.0148	
VBFNLO	0	-870.7			0.3176 ± 0.0051	unitarized, $\Lambda_{\mathrm{FF}} = 543$
VBFNLO	0	-435.3			0.3127 ± 0.0042	unitarized, $\Lambda_{\mathrm{FF}} = 637$
VBFNLO	0	-217.7			0.3094 ± 0.0060	unitarized, $\Lambda_{\mathrm{FF}} = 755$
VBFNLO	0	-108.8			0.3067 ± 0.0041	unitarized, $\Lambda_{\mathrm{FF}} = 905$
VBFNLO	0	108.8			0.3010 ± 0.0038	unitarized, $\Lambda_{\mathrm{FF}} = 905$
VBFNLO	0	217.7			0.3003 ± 0.0041	unitarized, $\Lambda_{\mathrm{FF}} = 755$
VBFNLO	0	435.3			0.3020 ± 0.0033	unitarized, $\Lambda_{\mathrm{FF}} = 637$
VBFNLO	0	870.7			0.3079 ± 0.0023	unitarized, $\Lambda_{\mathrm{FF}} = 543$
WHIZARD			0	0	0.3211 ± 0.0020	SM with Higgs
WHIZARD			0	0	0.3425 ± 0.0028	unitarized
WHIZARD			-0.4	0	0.9905 ± 0.0091	unitarized
WHIZARD			-0.2	0	0.6378 ± 0.0043	unitarized
WHIZARD			-0.1	0	0.4625 ± 0.0035	unitarized
WHIZARD			-0.05	0	0.4026 ± 0.0025	unitarized
WHIZARD			0.05	0	0.3230 ± 0.0018	unitarized
WHIZARD			0.1	0	0.3118 ± 0.0018	unitarized
WHIZARD			0.2	0	0.3256 ± 0.0019	unitarized
WHIZARD			0.4	0	0.3747 ± 0.0028	unitarized
WHIZARD			0	-0.4	1.0520 ± 0.0119	unitarized
WHIZARD			0	-0.2	0.6326 ± 0.0055	unitarized
WHIZARD			0	-0.1	0.4361 ± 0.0027	unitarized
WHIZARD			0	-0.05	0.3979 ± 0.0026	unitarized
WHIZARD			0	0.05	0.3632 ± 0.0020	unitarized
WHIZARD			0	0.1	0.4217 ± 0.0024	unitarized
WHIZARD			0	0.2	0.6499 ± 0.0060	unitarized
WHIZARD			0	0.4	0.9762 ± 0.0074	unitarized

Table B.1: List of all $W^{\pm}Z^{0}$ samples

Generator	f_0	f_1	α_4	α_5	cross section σ	comment
VBFNLO	0	0			0.6534 ± 0.0026	SM with Higgs
VBFNLO	0	0			0.6534 ± 0.0026	
VBFNLO	0	0			0.6534 ± 0.0026	unitarized
VBFNLO	-870.7	0			63.2299 ± 0.1589	
VBFNLO	-435.3	0			16.1029 ± 0.0606	
VBFNLO	-217.7	0			4.6573 ± 0.0206	
VBFNLO	-108.8	0			1.6768 ± 0.0091	
VBFNLO	108.8	0			1.5897 ± 0.0076	
VBFNLO	217.7	0			4.4911 ± 0.0158	
VBFNLO	435.3	0			16.4014 ± 0.0611	
VBFNLO	870.7	0			62.6464 ± 0.1557	
VBFNLO	-870.7	0			1.0048 ± 0.0033	unitarized, $\Lambda_{\mathrm{FF}} = 543$
VBFNLO	-435.3	0			0.8279 ± 0.0029	unitarized, $\Lambda_{\mathrm{FF}} = 637$
VBFNLO	-217.7	0			0.7410 ± 0.0027	unitarized, $\Lambda_{\mathrm{FF}} = 755$
VBFNLO	-108.8	0			0.6976 ± 0.0026	unitarized, $\Lambda_{\mathrm{FF}} = 905$
VBFNLO	108.8	0			0.6574 ± 0.0025	unitarized, $\Lambda_{\mathrm{FF}} = 905$
VBFNLO	217.7	0			0.6723 ± 0.0026	unitarized, $\Lambda_{\mathrm{FF}} = 755$
VBFNLO	435.3	0			0.7120 ± 0.0027	unitarized, $\Lambda_{\mathrm{FF}} = 637$
VBFNLO	870.7	0			0.8106 ± 0.0029	unitarized, $\Lambda_{\mathrm{FF}} = 543$
VBFNLO	1500	0			1.0477 ± 0.0037	unitarized, $\Lambda_{\mathrm{FF}} = 500$
VBFNLO	0	-653.1			35.9323 ± 0.1020	
VBFNLO	0	-435.3			16.4014 ± 0.0611	
VBFNLO	0	-217.7			4.6573 ± 0.0206	
VBFNLO	0	217.7			4.4911 ± 0.0158	
VBFNLO	0	435.3			16.1029 ± 0.0606	
VBFNLO	0	653.1			35.4844 ± 0.0990	
VBFNLO	0	-653.1			0.7026 ± 0.0026	unitarized, $\Lambda_{\mathrm{FF}} = 579$
VBFNLO	0	-435.3			0.6867 ± 0.0026	unitarized, $\Lambda_{\mathrm{FF}} = 637$
VBFNLO	0	-217.7			0.6709 ± 0.0026	unitarized, $\Lambda_{\mathrm{FF}} = 755$
VBFNLO	0	217.7			0.6504 ± 0.0026	unitarized, $\Lambda_{\mathrm{FF}} = 755$
VBFNLO	0	435.3			0.6524 ± 0.0026	unitarized, $\Lambda_{\mathrm{FF}} = 637$
VBFNLO	0	653.1			0.6559 ± 0.0026	unitarized, $\Lambda_{\mathrm{FF}} = 579$
WHIZARD			0	0	0.6606 ± 0.0012	SM with Higgs
WHIZARD			0	0	0.6410 ± 0.0105	
WHIZARD			0	0	0.6593 ± 0.0012	unitarized
WHIZARD			-0.4	0	117.0737 ± 5.7200	
WHIZARD			-0.2	0	28.8891 ± 1.3900	
WHIZARD			-0.1	0	6.7704 ± 0.2430	
WHIZARD			-0.05	0	2.2611 ± 0.0709	
WHIZARD			0.05	0	2.0733 ± 0.0607	
WHIZARD			0.1	0	7.8536 ± 0.3470	
WHIZARD			0.2	0	28.5528 ± 1.1200	
WHIZARD			0.4	0	105.8519 ± 5.4800	
WHIZARD			-0.4	0	3.4941 ± 0.0079	unitarized
WHIZARD			-0.2	0	2.0086 ± 0.0066	unitarized
WHIZARD			-0.1	0	1.2673 ± 0.0025	unitarized
WHIZARD			-0.05	0	0.9244 ± 0.0046	unitarized
WHIZARD			0.05	0	0.8554 ± 0.0017	unitarized
WHIZARD			0.1	0	1.1438 ± 0.0032	unitarized
WHIZARD			0.2	0	1.7867 ± 0.0051	unitarized
WHIZARD			0.4	0	3.0850 ± 0.0080	unitarized
WHIZARD			0	-0.3	19.8708 ± 1.2936	
WHIZARD			0	-0.2	8.4165 ± 0.3424	
WHIZARD			0	-0.1	2.6274 ± 0.0756	
WHIZARD			0	0.1	2.5140 ± 0.0834	
WHIZARD			0	0.2	6.5106 ± 0.2362	
WHIZARD			0	0.3	17.9422 ± 0.5513	
WHIZARD			0	-0.4	2.5736 ± 0.0054	unitarized
WHIZARD			0	-0.2	1.4781 ± 0.0031	unitarized
WHIZARD			0	-0.1	0.9953 ± 0.0018	unitarized
WHIZARD			0	-0.05	0.7980 ± 0.0016	unitarized
WHIZARD			0	0.05	0.7544 ± 0.0014	unitarized
WHIZARD			0	0.1	0.9171 ± 0.0022	unitarized
WHIZARD			0	0.2	1.3216 ± 0.0031	unitarized
WHIZARD			0	0.4	2.3265 ± 0.0053	unitarized

Table B.2: List of all same sign $W^{\pm}W^{\pm}$ samples

Appendix C

Other plots

The distributions shown in this thesis for other combinations of channels and parameters are listed here. Other distributions of differential cross sections are shown at:

`www.iktp.tu-dresden.de/~bittrich/BA-results/Rivet/index.html`

C.1 Total cross section plots

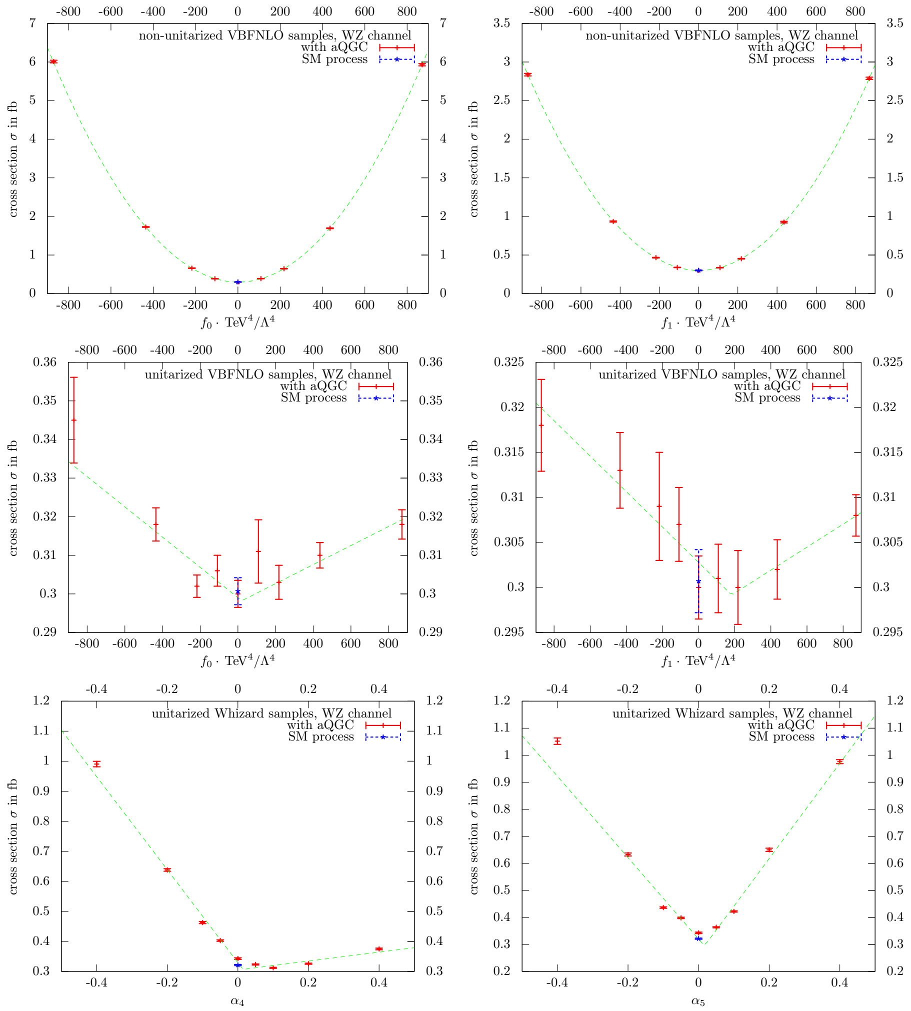

Figure C.1: Dependency of total cross sections on the aQGC parameter for different samples in the WZ channel. For further information see next figure.

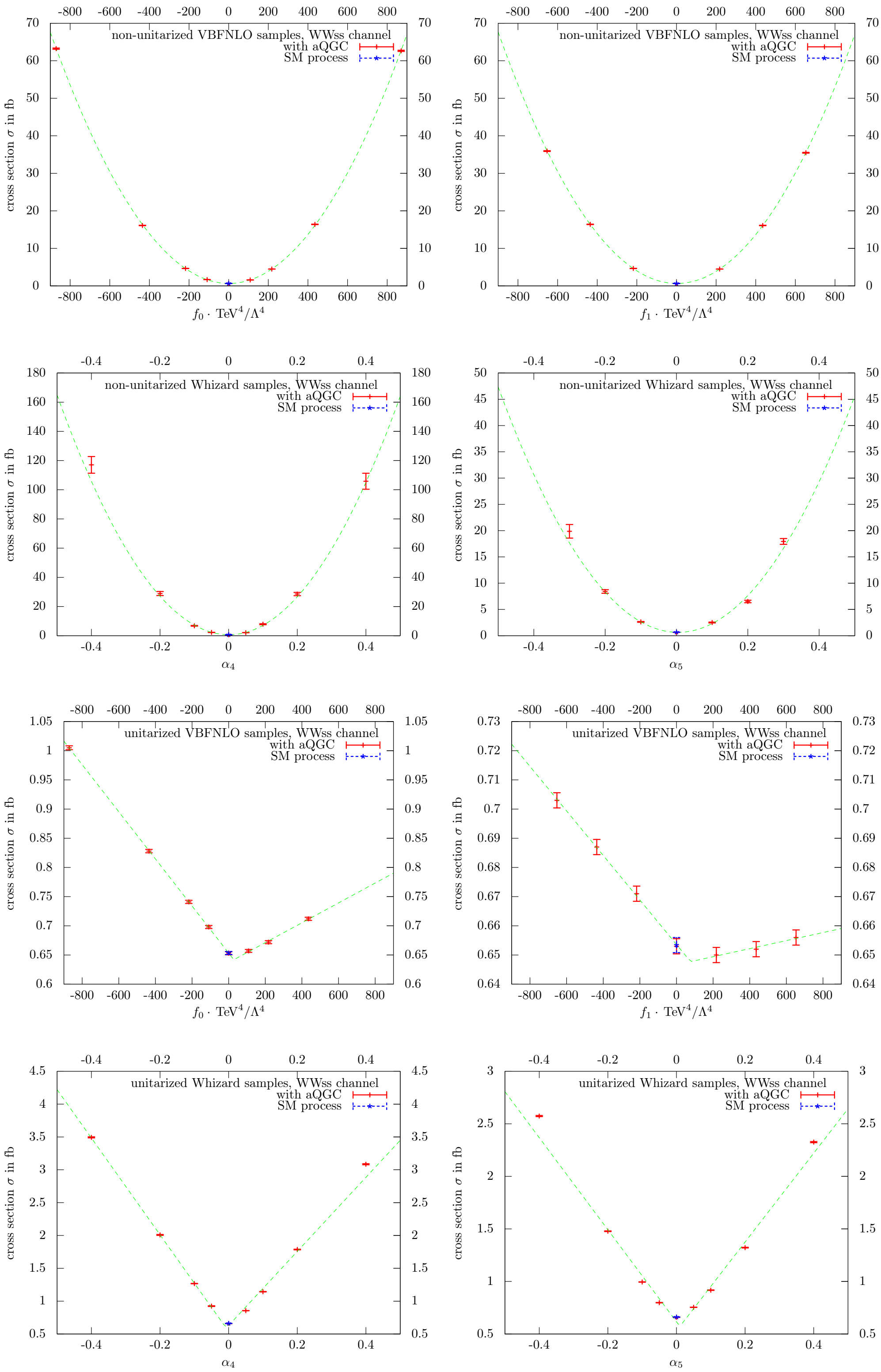

Figure C.2: Dependency of σ on the aQGC parameter f_0 for the WWss channel. Red crosses correspond to the cross sections of the generated samples. Blue data points refer to the cross section of the samples generated using the mode for the SM process. The green dashed line is a parabolic fit for non-unitarized samples. For the unitarized samples it is a combination of two linear fits with independet slopes for different values for the aQGC parameter.

C.2 Differential cross section plots

C.2.1 WWss channel

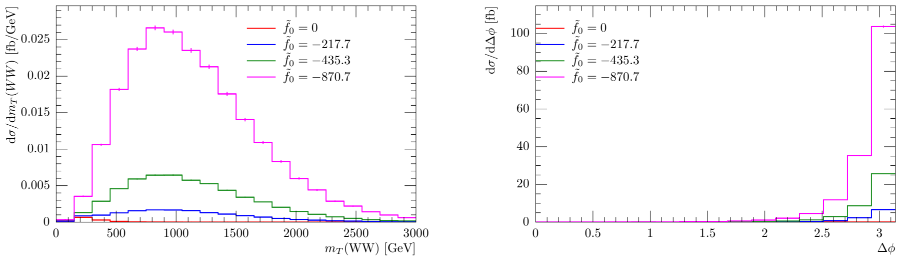

Figure C.3: Comparison of different values for aQGC parameter f_0, with $f_1 = 0$, in the `WWss` channel. No unitarization was used. The left distribution shows the differential cross section over the transverse mass of the pair of vector bosons $m_{\mathrm{T}}(WW)$. The right distribution shows the differential cross section dependency on the absolute value of the angle between the projections of the leptons' momenta in the x-y plane $\Delta\phi(\ell\ell)$. The different colors represent different values for $\tilde{f}_0$ as listed in the key.

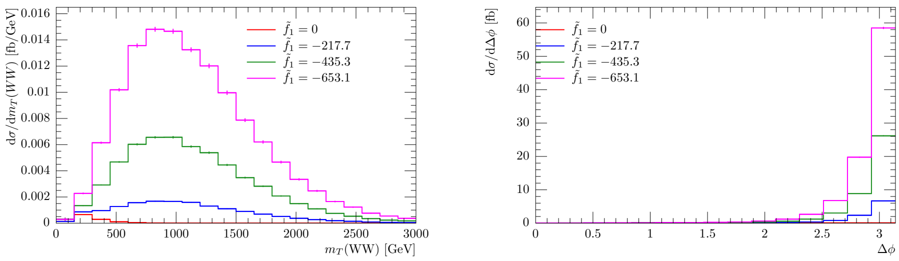

Figure C.4: Comparison of different values for aQGC parameter f_1, with $f_0 = 0$, in the `WWss` channel. No unitarization was used. The left distribution shows the differential cross section over the transverse mass of the pair of vector bosons $m_{\mathrm{T}}(WW)$. The right distribution shows the differential cross section dependency on the absolute value of the angle between the projections of the leptons' momenta in the x-y plane $\Delta\phi(\ell\ell)$. The different colors represent different values for $\tilde{f}_0$ as listed in the key.

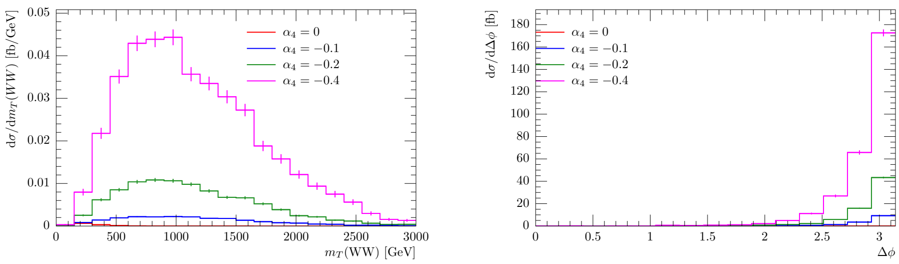

Figure C.5: Comparison of different values for aQGC parameter α_0, with $\alpha_1 = 0$, in the `WWss` channel. No unitarization was used. The left distribution shows the differential cross section over the transverse mass of the pair of vector bosons $m_{\mathrm{T}}(WW)$. The right distribution shows the differential cross section dependency on the absolute value of the angle between the projections of the leptons' momenta in the x-y plane $\Delta\phi(\ell\ell)$. The different colors represent different values for $\tilde{f}_0$ as listed in the key.

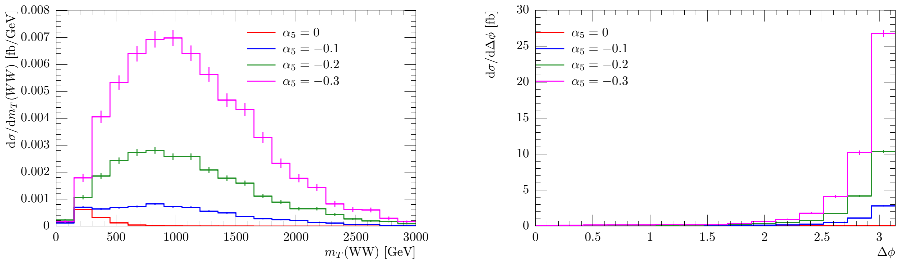

Figure C.6: Comparison of different values for aQGC parameter α_1, with $\alpha_0 = 0$, in the `WWss` channel. No unitarization was used. The left distribution shows the differential cross section over the transverse mass of the pair of vector bosons $m_{\mathrm{T}}(WW)$. The right distribution shows the differential cross section dependency on the absolute value of the angle between the projections of the leptons' momenta in the x-y plane $\Delta\phi(\ell\ell)$. The different colors represent different values for $\tilde{f}_0$ as listed in the key.

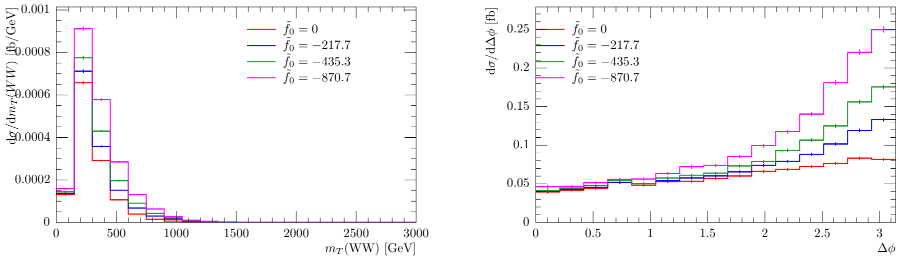

Figure C.7: Comparison of different values for aQGC parameter f_0, with $f_1 = 0$, in the `WWss` channel. Unitarization was applied. The left distribution shows the differential cross section over the transverse mass of the pair of vector bosons $m_{\mathrm{T}}(WW)$. The right distribution shows the differential cross section dependency on the absolute value of the angle between the projections of the leptons' momenta in the x-y plane $\Delta\phi(\ell\ell)$. The different colors represent different values for $\tilde{f}_0$ as listed in the key.

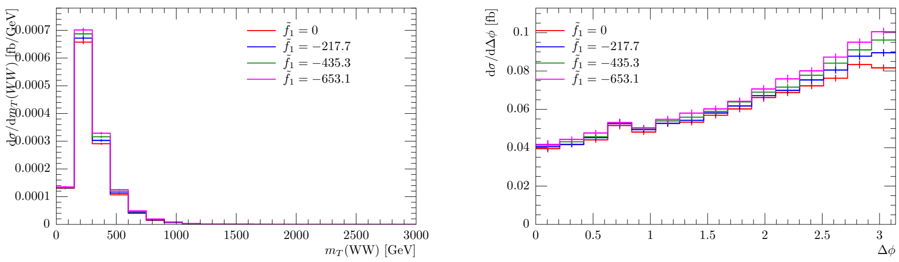

Figure C.8: Comparison of different values for aQGC parameter f_1, with $f_0 = 0$, in the `WWss` channel. Unitarization was applied. The left distribution shows the differential cross section over the transverse mass of the pair of vector bosons $m_{\mathrm{T}}(WW)$. The right distribution shows the differential cross section dependency on the absolute value of the angle between the projections of the leptons' momenta in the x-y plane $\Delta\phi(\ell\ell)$. The different colors represent different values for $\tilde{f}_0$ as listed in the key.

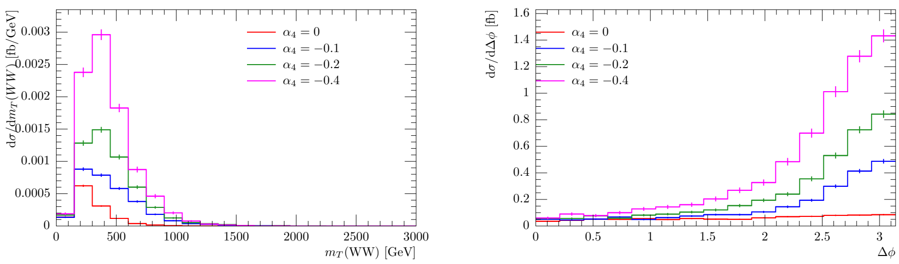

Figure C.9: Comparison of different values for aQGC parameter α_4, with $\alpha_5 = 0$, in the WWss channel. Unitarization was applied. The left distribution shows the differential cross section over the transverse mass of the pair of vector bosons $m_{\mathrm{T}}(WW)$. The right distribution shows the differential cross section dependency on the absolute value of the angle between the projections of the leptons' momenta in the x-y plane $\Delta\phi(\ell\ell)$. The different colors represent different values for $\tilde{f}_0$ as listed in the key.

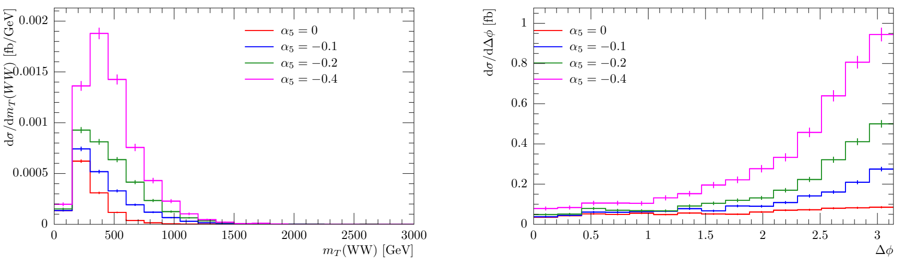

Figure C.10: Comparison of different values for aQGC parameter α_5, with $\alpha_4 = 0$, in the WWss channel. Unitarization was applied. The left distribution shows the differential cross section over the transverse mass of the pair of vector bosons $m_{\mathrm{T}}(WW)$. The right distribution shows the differential cross section dependency on the absolute value of the angle between the projections of the leptons' momenta in the x-y plane $\Delta\phi(\ell\ell)$. The different colors represent different values for $\tilde{f}_0$ as listed in the key.

C.2.2 WZ channel

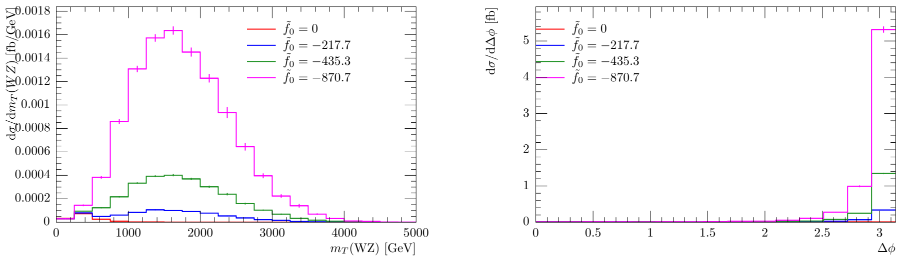

Figure C.11: Comparison of different values for aQGC parameter f_0, with $f_1 = 0$, in the `WZ` channel. No unitarization was used. The left distribution shows the differential cross section over the transverse mass of the pair of vector bosons $m_\mathrm{T}(WZ)$. The right distribution shows the differential cross section dependency on the absolute value of the angle between the projections of the vector bosons' momenta in the x-y plane $\Delta\phi(WZ)$. The different colors represent different values for $\tilde{f}_0$ as listed in the key.

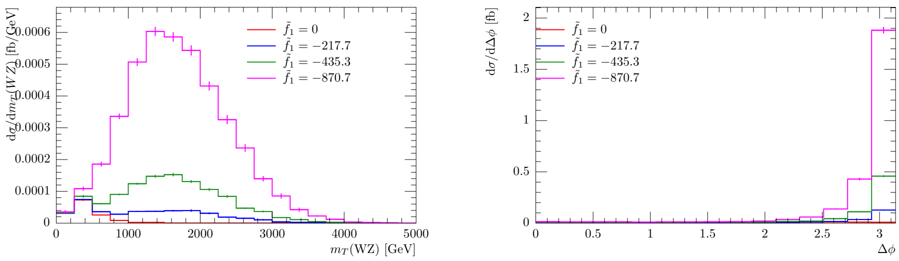

Figure C.12: Comparison of different values for aQGC parameter f_1, with $f_0 = 0$, in the `WZ` channel. No unitarization was used. The left distribution shows the differential cross section over the transverse mass of the pair of vector bosons $m_\mathrm{T}(WZ)$. The right distribution shows the differential cross section dependency on the absolute value of the angle between the projections of the vector bosons' momenta in the x-y plane $\Delta\phi(WZ)$. The different colors represent different values for $\tilde{f}_0$ as listed in the key.

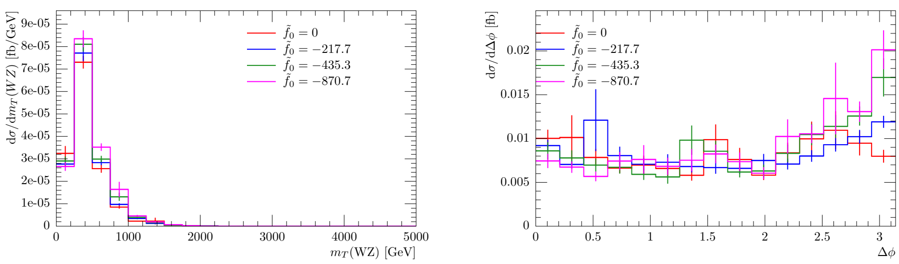

Figure C.13: Comparison of different values for aQGC parameter f_0, with $f_1 = 0$, in the `WZ` channel. Unitarization was applied. The left distribution shows the differential cross section over the transverse mass of the pair of vector bosons $m_\mathrm{T}(WZ)$. The right distribution shows the differential cross section dependency on the absolute value of the angle between the projections of the vector bosons' momenta in the x-y plane $\Delta\phi(WZ)$. The different colors represent different values for $\tilde{f}_0$ as listed in the key.

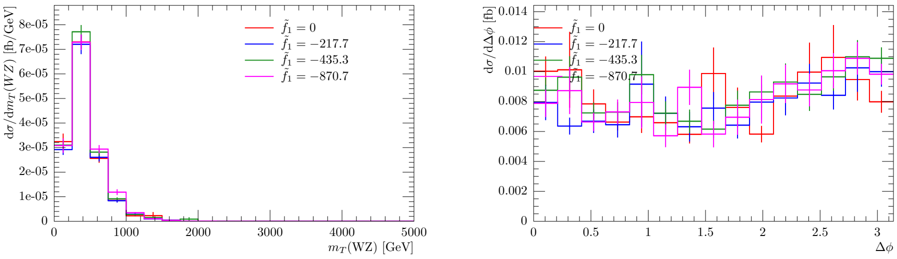

Figure C.14: Comparison of different values for aQGC parameter f_1, with $f_0 = 0$, in the WZ channel. Unitarization was applied. The left distribution shows the differential cross section over the transverse mass of the pair of vector bosons $m_{\mathrm{T}}(WZ)$. The right distribution shows the differential cross section dependency on the absolute value of the angle between the projections of the vector bosons' momenta in the x-y plane $\Delta\phi(WZ)$. The different colors represent different values for $\tilde{f}_0$ as listed in the key.

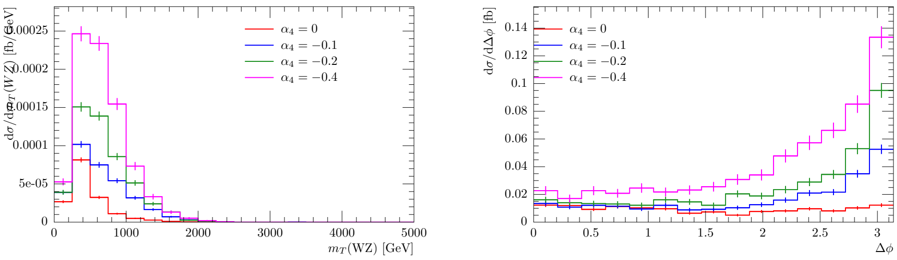

Figure C.15: Comparison of different values for aQGC parameter α_4, with $\alpha_5 = 0$, in the WZ channel. Unitarization was applied. The left distribution shows the differential cross section over the transverse mass of the pair of vector bosons $m_{\mathrm{T}}(WZ)$. The right distribution shows the differential cross section dependency on the absolute value of the angle between the projections of the vector bosons' momenta in the x-y plane $\Delta\phi(WZ)$. The different colors represent different values for $\tilde{f}_0$ as listed in the key.

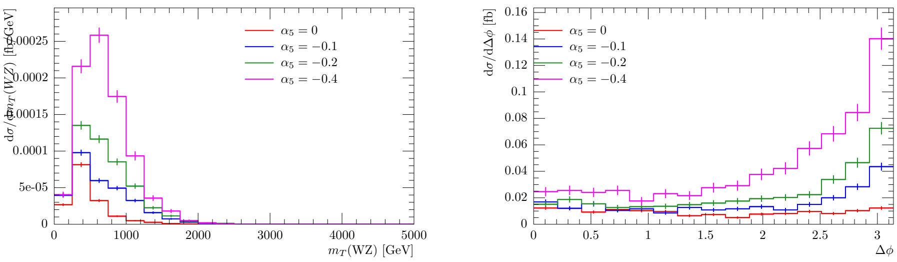

Figure C.16: Comparison of different values for aQGC parameter α_5, with $\alpha_4 = 0$, in the WZ channel. Unitarization was applied. The left distribution shows the differential cross section over the transverse mass of the pair of vector bosons $m_{\mathrm{T}}(WZ)$. The right distribution shows the differential cross section dependency on the absolute value of the angle between the projections of the vector bosons' momenta in the x-y plane $\Delta\phi(WZ)$. The different colors represent different values for $\tilde{f}_0$ as listed in the key.

C.3 Conversion between different parametrizations

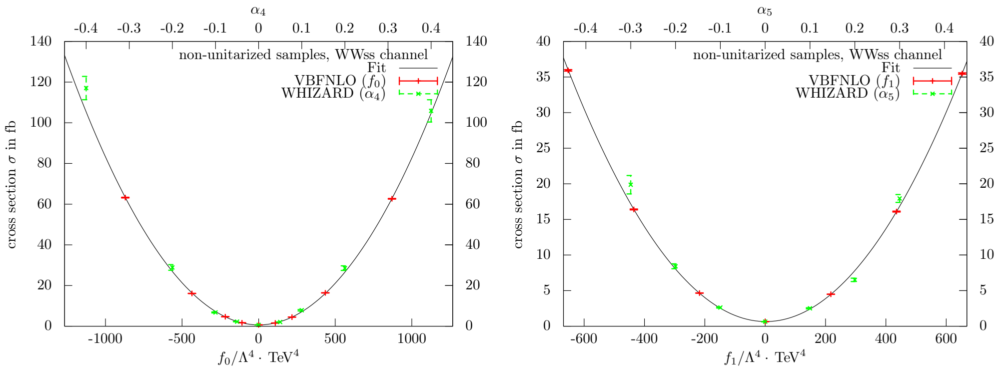

Figure C.17: Dependency of σ on the aQGC parameter f_i and α_{i+4} for the `WWss` channel, non-unitarized samples. Left: parameters f_0 and α_4. Right: parameters f_1 and α_5. Red crosses correspond to the cross sections of the samples generated by VBFNLO. Green data points refer to the cross section of the samples generated by WHIZARD. The black line is a parabolic fit for all samples. f_i-axis was scaled to match α_{i+4}-axis according to fit parameter t_i.

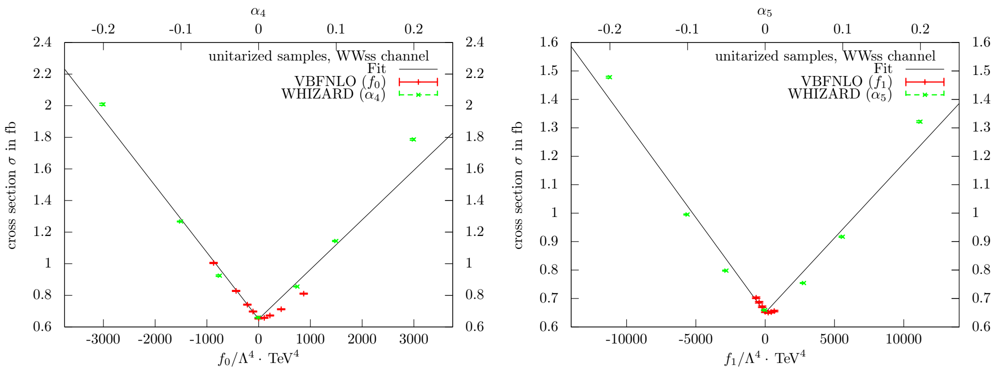

Figure C.18: Dependency of σ on the aQGC parameter f_i and α_{i+4} for the `WWss` channel, unitarized samples. Left: parameters f_0 and α_4. Right: parameters f_1 and α_5. Red crosses correspond to the cross sections of the samples generated by VBFNLO. Green data points refer to the cross section of the samples generated by WHIZARD. The black line is a fit for all samples according to equation(8.1). f_i-axis was scaled to match α_{i+4}-axis according to fit parameter t_i.

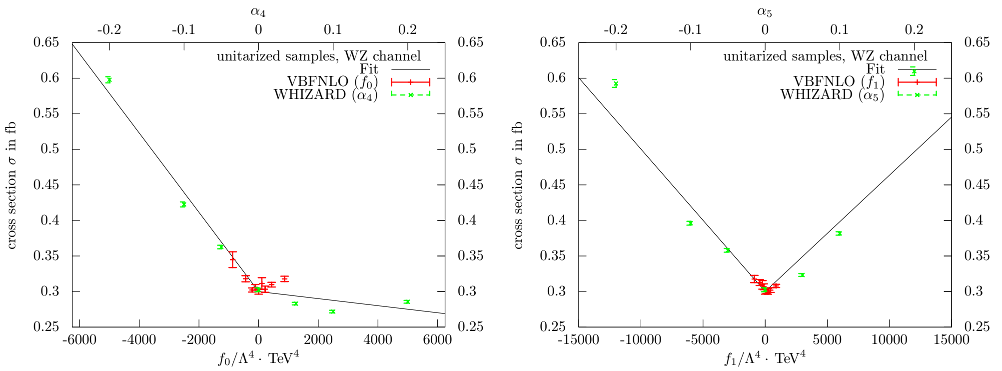

Figure C.19: Dependency of σ on the aQGC parameter f_i and α_{i+4} for the `WWss` channel, unitarized samples. Left: parameters f_0 and α_4. Right: parameters f_1 and α_5. Red crosses correspond to the cross sections of the samples generated by VBFNLO. Green data points refer to the cross section of the samples generated by WHIZARD. The black line is a fit for all samples according to equation(8.1). f_i-axis was scaled to match α_{i+4}-axis according to fit parameter t_i.

C.3.1 differential cross sections for similar total cross sections

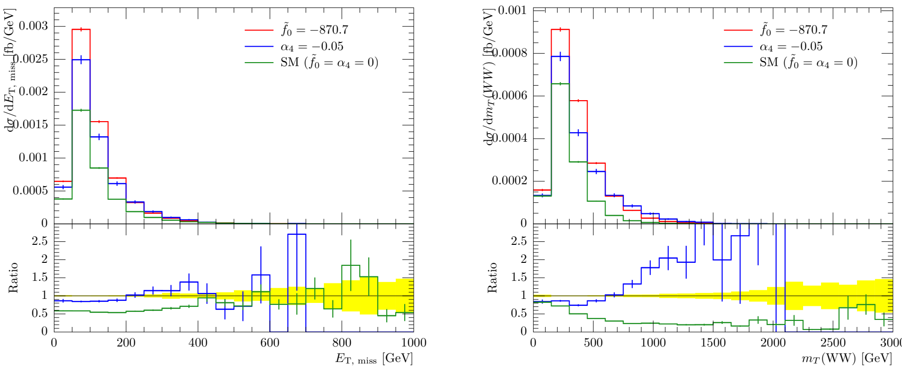

Figure C.20: Comparison of values for aQGC parameter f_0 and α_4, with similar cross section, with $f_1 = \alpha_5 = 0$, in the `WWss` channel. Unitarization was applied. The left distribution shows the differential cross section over E_T^{miss}. The right distribution shows the differential cross section dependency on the invariant mass of the vector boson pair $m_T(WW)$.

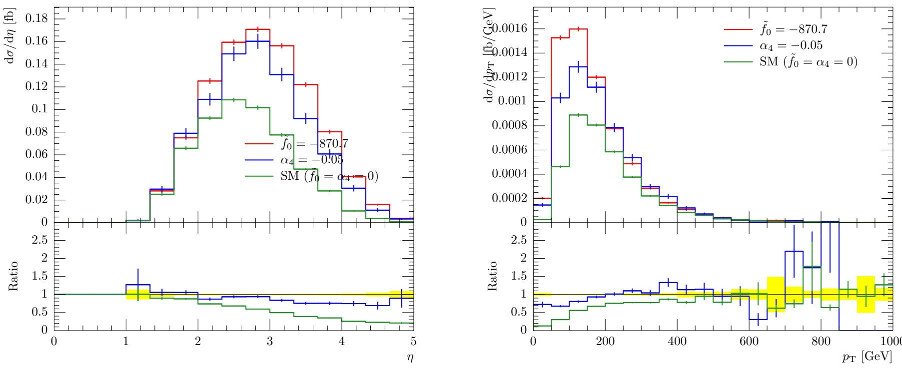

Figure C.21: Comparison of values for aQGC parameter f_0 and α_4, with similar cross section, with $f_1 = \alpha_5 = 0$, in the `WWss` channel. Unitarization was applied. The left distribution shows the differential cross section over $|\eta|$ of the most forward jet. The right distribution shows the differential cross section dependency on the transverse momentum of the leading jet $p_T(j_1)$.

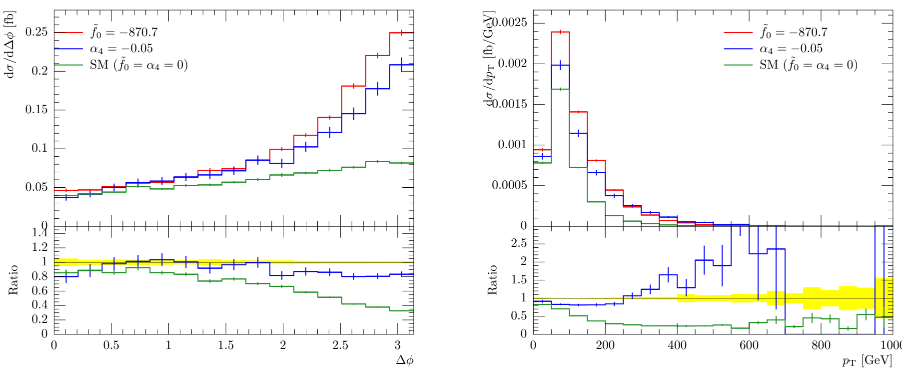

Figure C.22: Comparison of values for aQGC parameter f_0 and α_4, with similar cross section, with $f_1 = \alpha_5 = 0$, in the `WWss` channel. Unitarization was applied. The left distribution shows the differential cross section over $|\Delta\phi(\ell\ell)|$ of the most forward lepton. The right distribution shows the differential cross section dependency on the transverse momentum of the leading lepton $p_T(\ell_1)$.

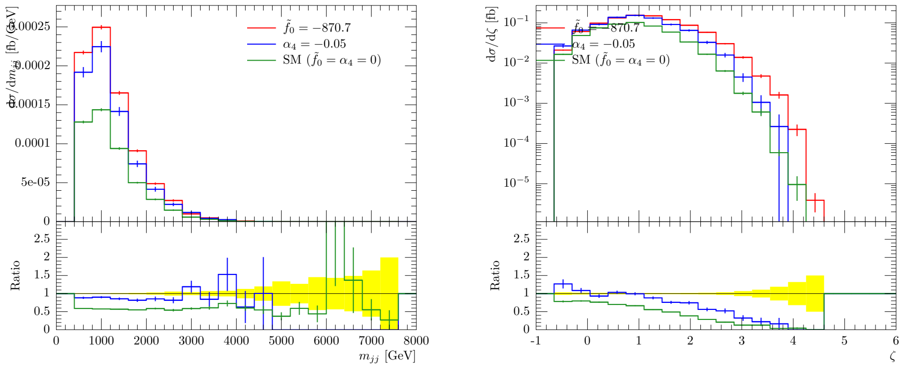

Figure C.23: Comparison of values for aQGC parameter f_0 and α_4, with similar cross section, with $f_1 = \alpha_5 = 0$, in the `WWss` channel. Unitarization was applied. The left distribution shows the differential cross section over the invariant mass of the jet pair M_{jj}. The right distribution shows the differential cross section dependency on the transverse momentum of the lepton centrality ζ.

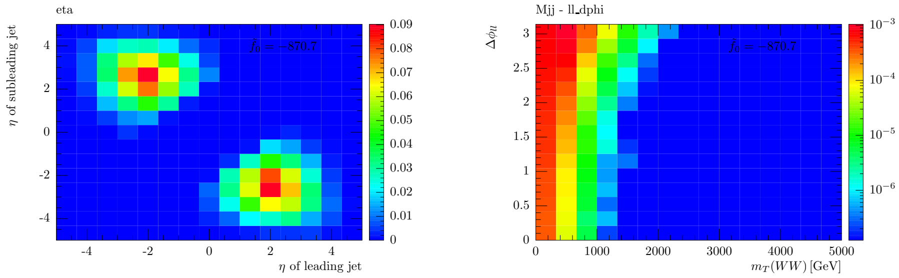

Figure C.24: Two-dimensional distributions for unitarized `WWss` samples with $\tilde{f}_0 = -870.7$. The left distribution shows a two-dimensional distribution of η of the lets. x-axis represents the absolute value of the pseudorapidity of the leading jet, while the y-axis corresponds to the subleading jet. The right distribution shows a two-dimensional distribution of the transverse mass of the vector boson pair $m_{\mathrm{T}}(WW)$ and the difference of the angle $|\Delta\phi_{\ell\ell}|$.

Bibliography

[1] O. J. P. Eboli, M. C. Gonzalez-Garcia, and J. K. Mizukoshi, *$pp \to jje^{\pm}\mu^{\pm}\nu\nu$ and $jje^{\pm}\mu^{\mp}\nu\nu$ at $\mathcal{O}(\alpha_{em}^6)$ and $\mathcal{O}(\alpha_{em}^4\alpha_s^2)$ for the Study of the Quartic Electroweak Gauge Boson Vertex at LHC*, arXiv.org **hep-ph** (2006).

[2] S. Weinberg, *A Model of Leptons*, Phys. Rev. Lett. **19** (1967) 1264–1266.

[3] A. Salam, *Elementary Particle Theory*, Almqvist and Wiksell (1968).

[4] S. L. Glashow, *Partial-Symmetries of Weak Interactions*, Nuclear Physics **22** (1961) 579–588.

[5] J. Beringer et al (Particle Data Group), *The Review of Particle Physics*, Physical Review D **86** (2012) 010001.

[6] T. A. Collaboration, *Observation of a new particle in the search for the Standard Model Higgs boson with the ATLAS detector at the LHC*, arXiv.org **hep-ex** (2012).

[7] P. W. Higgs, *Broken Symmetries and the Masses of Gauge Bosons*, Phys.Rev.Lett. **13** (1964) 508–509.

[8] P. W. Higgs, *Spontaneous Symmetry Breakdown without Massless Bosons*, Phys.Rev. **145** (1966) 1156–1163.

[9] A. Alboteanu, W. Kilian, and J. Reuter, *Resonances and Unitarity in Weak Boson Scattering at the LHC*, arXiv.org **hep-ph** (2008).

[10] J. Schumacher, M. Kobel, and N. Wermes, *Sensitivity of ATLAS to Alternative Mechanisms of Electroweak Symmetry Breaking in Vector Boson Scattering $qq \to qql\nu l\nu$.* . PhD thesis, Bonn, Universität Bonn, Bonn, 2010.

[11] C. Degrande, N. Greiner, W. Kilian, O. Mattelaer, H. Mebane, T. Stelzer, S. Willenbrock, and C. Zhang, *Effective Field Theory: A Modern Approach to Anomalous Couplings*, arXiv.org **hep-ph** (2012).

[12] S. D. Rindani, *Strong gauge boson scattering at the LHC*, arXiv.org **hep-ph** (2009).

[13] B. Feigl, *Anomale Vier-Vektorboson-Kopplungen bei der Produktion von drei Vektorbosonen am LHC*, Master's thesis, Karlsruher Institut für Technologie, Karlsruhe.

[14] T. S. Pettersson and P. Lefèvre, *The Large Hadron Collider: conceptual design. oai:cds.cern.ch:291782*, Tech. Rep. CERN-AC-95-05 LHC, CERN, Geneva, Oct, 1995.

[15] A. Horvath, *schematical overview of LHC for Wikipedia*, Nov., 2012. `http://commons.wikimedia.org/wiki/File:LHC.svg`.

[16] *public luminosity results*, Nov., 2012. `https://twiki.cern.ch/twiki/bin/view/AtlasPublic/LuminosityPublicResults`.

[17] G. Aad et al, *The ATLAS Experiment at the CERN Large Hadron Collider*, J. Instrum. **3** (2008) S08003. 437 p.

[18] M. Dobbs, J. B. Hanse, L. Garren, and L. Sonnenschein, *a C++ Event Record for Monte Carlo Generators.* Victoria, Canada, May, 2010.

[19] K. Arnold et al, *VBFNLO: A parton level Monte Carlo for processes with electroweak bosons – Manual for Version 2.6.0*, arXiv.org **hep-ph** (2011).

[20] W. Kilian, T. Ohl, and J. Reuter, *WHIZARD: Simulating Multi-Particle Processes at LHC and ILC*, arXiv.org **hep-ph** (2007).

[21] A. Buckley et al, *Rivet user manual*, arXiv.org **hep-ph** (2010).

[22] *Expected photon performance in the ATLAS experiment*, Tech. Rep. ATL-PHYS-PUB-2011-007, CERN, Geneva, Apr, 2011.

[23] P. Anger, M. Kobel, K. Zuber, and A. Vest, *Study of Vector Boson Scattering with Pile-up with the ATLAS Detector at the LHC.* , Master's thesis, Dresden, TU Dresden, Dresden, 2010.

Erklärung

Hiermit erkläre ich, dass ich diese Arbeit im Rahmen der Betreuung am Institut für Kern- und Teilchenphysik ohne unzulässige Hilfe Dritter verfasst und alle Quellen als solche gekennzeichnet habe.

Carsten Bittrich
Dresden, Dezember 2012